Master’s thesis
Master’s Degree in Mechanical Engineering

Computational Fluid Dynamics Analysis of a Bus Cooling System

By
Tural Suleymanov

Supervisors:
Prof .Delprete Cristiana
Prof. Huseyin Pahlivan

Politecnico di Torino
2022

Declaration

I hereby declare that the contents and organization of this dissertation constitute my own original work and does not compromise in any way the rights of third parties, including those relating to the security of personal data.

Tural Suleymanov

2022

I would like to dedicate this thesis to my loving mother who dedicated her entire life for education of her children.

Acknowledgment

First and foremost I am extremely grateful to my supervisors, Prof. Delprete Cristiana and Prof. Huseyin Pahlivan for their invaluable advice, continuous support, and patience during my Master's study. Their immense knowledge and plentiful experience have encouraged me all the time in my academic research and daily life. I would like to express gratitude to my friend, Dr. Elshad Valiyev, for his treasured support which was influential in shaping my experiment methods and critiquing my results. My appreciation also goes out to my family and friends for their encouragement and support all through my studies.

ABSTRACT

The paper examines the Computational Fluid Dynamics analysis of a bus air conditioning system. The bus under examination has a capacity of 29 sitting and 25 standing passengers. The effectiveness and efficiency of the system were analyzed through the Anasys Fluent software. During the study, the experimental results were put in comparison with the outcome of CFD results.

For clarity of CFD results and to reach a significantly close outcome, different error elimination techniques, such as Mesh error elimination, were applied for the betterment of the work. Besides, to be precise, two different turbulence models, k-ϵ Standart and k-ω SST models were applied to the indicated system for deduction of a suitable method. The air conditioning system is used to decrease the inner temperature of the bus from 30 to 16 C°. Therefore, the inlet temperature in the analysis was set to 16 C°. The experiments were conducted by the anemometer of the KIMO VT200 brand. The test was conducted on the left side of the bus and measurements were conducted on every outlet section and the effectiveness of the system was investigated.

Finally, a suggested air optimal air channel design was proposed and CFD analysis results for the suggested system were demonstrated.

Table of Contents

List of Figures

List of Tables

Chapter 1

Introduction

In this chapter general information about commonness, design criteria, and working principles of mobile air conditioning systems is examined. Besides, the differences between residential and mobile AC systems are studied. Furthermore, information about bus body construction and insulation materials was dedicated. As a final point, general information, history, and application fields of Computational Fluid dynamics are indicated.

1.1 Mobile air conditioning systems

Public transportation plays a significant role in the daily life of societies as it provides people with mobility and access to employment, community resources, medical care, and recreational opportunities. The usage of buses yields several benefits in different aspects such as community health, reduced air pollution, fuel efficiency, road congestion, etc.

Besides affordability, another aspect which also notable is comfort. At this point, the air conditioning system comes into play as it is commonly associated with comfort. Below the graph, we see the number of cars equipped with air conditioning systems between the years 1992 and 2004 As it can be seen clearly from the figure, the number of cars equipped with air conditioners has increased significantly (Daly, 2006).

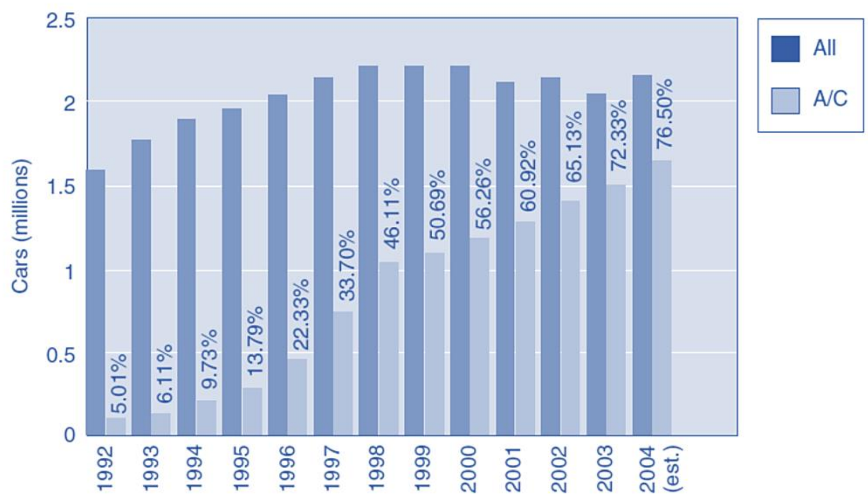

Figure 1.1 Number of vehicles equipped with A/C between 1992 to 2004.

Currently, this number is above 95% and A/C is accepted to be the standard option for all types of vehicles (Kaynaklıand Horuz, 2003).

1.1.1 The differences between mobile and stationary AC systems

With the evolution of science and engineering, several improvements were done to air conditioning systems over the course of years. The mobile A/C systems, operation vise, are considerably different from the residential types. There are several factors such as the ambient temperature, solar radiation, and vehicle speed which have a big impact on the system performance (Qi et. al., 2007). Other aspects of differences between mobile and residential types lies on the thermal environment differences.

- Volume occupation per human is significantly smaller
- Microclimate parameters can change rapidly by changing car orientation
- Cabin interiors possess a complex shape
- Surfaces near passengers sitting zones can have higher or lower temperatures than the overall interior temperature
- Position change of passengers within the cabin can be impossible or limited
- Large glazing areas with respect to overall cabin surface (Ruzic, 2011).

Nonetheless, conditions of thermal comfort in vehicles should be the same as in apartments. In bus air conditioners not only the power of the system but also its distribution plays a significant role. For the appropriate distribution of cooled air in passenger cabins, special distribution channels have been designed by different brands. The aim of these channels is to equate the overall temperature of different regions inside a bus, and thus, achieve the desired level of comfort for passengers. Briefly, airflow velocity and uniform distribution inside the vehicle possess high importance thermal comfort of the passengers. (Mezarciöz, 2015).

1.1.2 Conditions for thermal comfort

Besides, the air conditioning of the bus cabins, where people travel in groups, is very important in terms of comfort, hygiene, and safety. Briefly, as in every living area, the purpose of air conditioning in buses is to heat, cool, keep the humidity at appropriate values, and provide a clean indoor environment. There are six main factors to consider when defining conditions for thermal comfort (Valiyev, 2021).

- Metabolic rate
- Clothing insulation
- Temperature

- Radiant temperature
- Air speed
- Humidity (Standard, 2010, p. 4)

1.1.3 Mobile AC design criteria

As air mobile air conditioners have different working conditions, there are several factors that must be obeyed during the design procedure of air-conditioning systems for busses.

- Design conditions showing outdoor temperature and contaminants
- The effect of the air conditioning system on the engine
- Effect of sun rays and noise
- Flexibility and robustness of vehicle body structure
- For the comfort of passengers, the presence of thermal insulation and absence of air leakages
- Presence of the required electrical power and cooling capacity (ASGHAR, 2016, s. 8).

1.1.4 Types of AC for busses

Keeping the working principle, as shown above, there can be two different installations of AC systems in busses, integrated and rooftop units. Integrated ones can be installed on the luggage rack. A rooftop unit is installed on top of a vehicle (Mezarciöz, 2015). Below in the photos, we see Integrated and Rooftop models respectively.

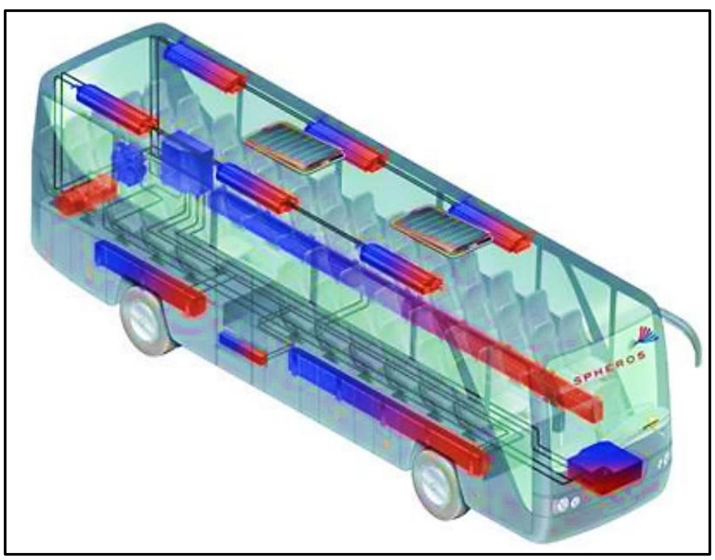

Figure 1.2 Bus with Integrated cooling system

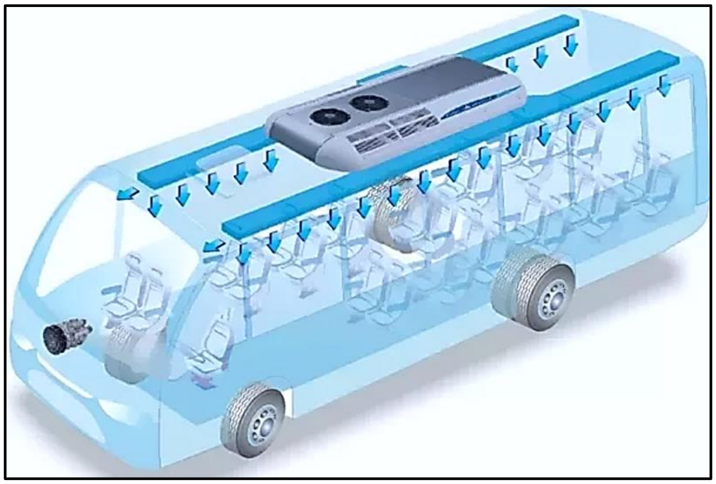

Figure 1.3 Bus with Rooftop cooling system

Recently, the usage of rooftop air conditioning systems has comparatively increased. To ensure constant operation of AC, auxiliary engines are quite commonly used (Mansour et. al., 2007). In rooftop AC, almost all of the elements except for the compressor, are installed on the top of a vehicle. The compressor is installed in the engine room and is driven by engine (Mezarciöz, 2015).

1.2 Working scheme of AC in busses

There are several types of air conditioning systems designed for buses, however, the working principle in all cases is quite similar. On the rare part of a bus generally, there is a compressor that sucks in a gaseous refrigerant and compresses it. To switch the compression on and off there is an electromagnetic clutch attached to the frontal part of the compressor.

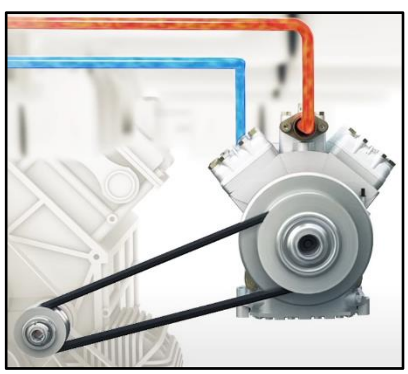

Figure 1.4 AC compressor for busses

The compressed fluid at the compressor is sent to the condenser where it is being condensed and heat is drawn from it. A condenser's purpose is to transfer heat from a working fluid to the ambient air. The effective heat transfer that takes place during phase shifts, in this example during the condensation of vapor into a liquid, is what powers the condenser.

Figure 1.5 AC condenser

After leaving the condenser the refrigerant enters the refrigerant receiver depending on the working mode of the system, the required amount of refrigerant is sent to the expansion valve.

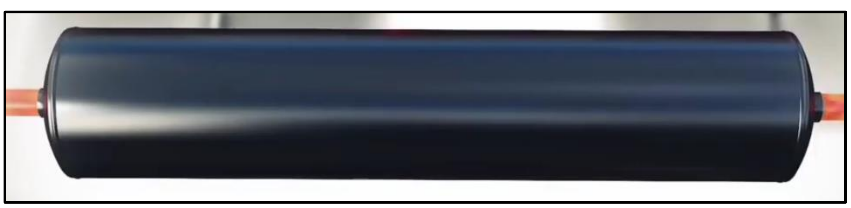

Figure 1.6 AC Refrigerant receiver

After leaving the refrigerant receiver, fluid enters the filter drier. In an air conditioning system, a filter-drier serves two crucial purposes: first, it adsorbs system contaminants like water, which can produce acids, and second, it offers physical filtering. Each component must be evaluated to guarantee optimal and cost-effective dryer design.

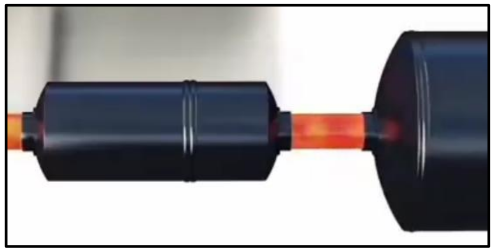

Figure 1.7 AC Filter drier

On the tubing from the filter drier to the expansion valve, there is a solenoid valve which if needed stops the flow of refrigerant to the evaporator by turning off the compressor. The typically closed form of the solenoid is the most prevalent variety. The valve opens as soon as the coil is powered up. The valve closes when the power is turned off. When power is provided to the coil in a typically open solenoid, the valve shuts, and when the coil is de-energized, it opens.

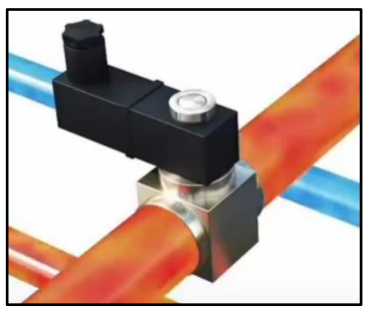

Figure 1.8 AC Solenoid valve

Before entering the evaporator, the refrigerant amount is regulated by the expansion valve and only the required amount enters it. The refrigerant would pour into the evaporator coil without losing any pressure if there was no expansion valve. Only a limited portion of the refrigerant is allowed to enter the coil due to the expansion valve. This refrigerant finds itself suddenly allowed to spread out in the comparatively empty evaporator coil when it arrives.

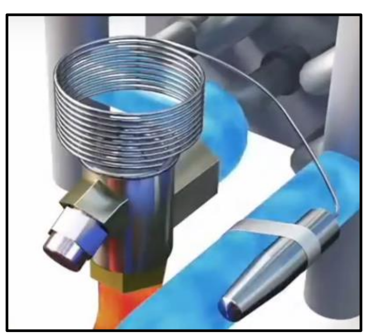

Figure 1.9 AC Expansion valve

After liquid refrigerant enters the evaporator, it is spread inside it. Required heat for the evaporation process is withdrawn from the air. As a result of this process, the air around the evaporator acquired a reduction in temperature. The cooled air, with the help of fans, is sucked and then blown into the channels on both sides of a bus.

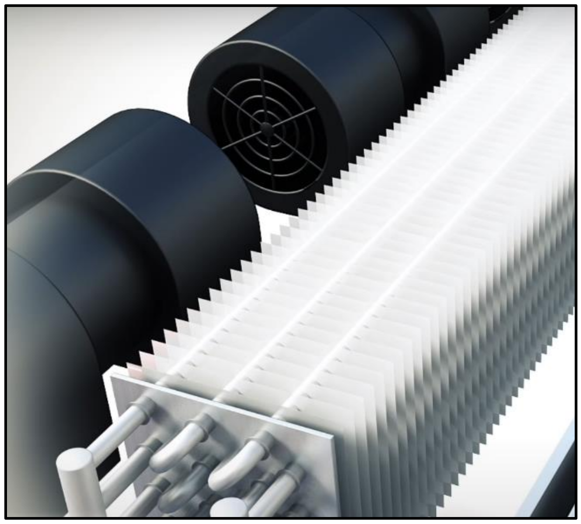

Figure 1.10 AC Evaporator and fans

Through the outlet sections of the channels, the cooled air is evenly distributed into the passenger cabin.

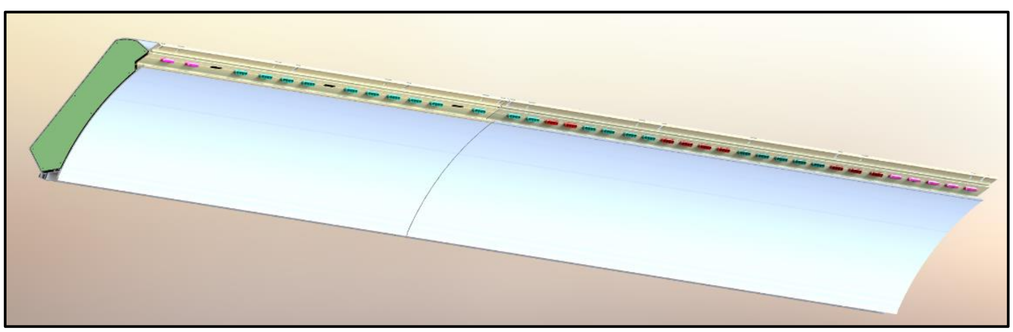

Figure 1.11 AC Air channel

There can be cases when instead of one condenser, two condensers are used. However, when there are two condensers, they are connected in series which allows the condensation process to take place in two stages. Nevertheless, evaporators are connected in parallel which allows equivalent cooling conditions for both passenger rows (Mansour et. Al., 2007).

1.2.1 AC fuel consumption

Fuel consumption of AC systems is another aspect that can't be underestimated. AC is the second most energy-consuming part of a vehicle. In a system where AC is driven by the engine, the driver can feel the drop in power of a vehicle when AC electromagnetic clutch is engaged (Mansour et. al., 2007). In the United State, approximately 26 billion liters of fuel are consumed each year for vehicle inner cooling (Rugh and Hovland, 2003).

The high dependency on petroleum resources will make it deplete in the next 40 years, therefore, there is a ceaseless improvement in the automative sector. Also, AC manufacturers put emphasis on increasing of efficiency of systems without forfeiting passengers' thermal comfort (Mansour et. Al., 2007).

1.3 Bus body structure

The bus body can be divided into three parts: chassis and engine, structural body, and interior, and exterior parts. The chassis and engine are very important. They are required to pass the standard exam by domestic and international organizations. The chassis consists of two main types: one piece and three joint13 combination pieces. The one-piece chassis is used for the single-decker medium bus size, while the three combination pieces are used for the long bus size or double-decker bus. (S. Butdee, 2008, p. 458)

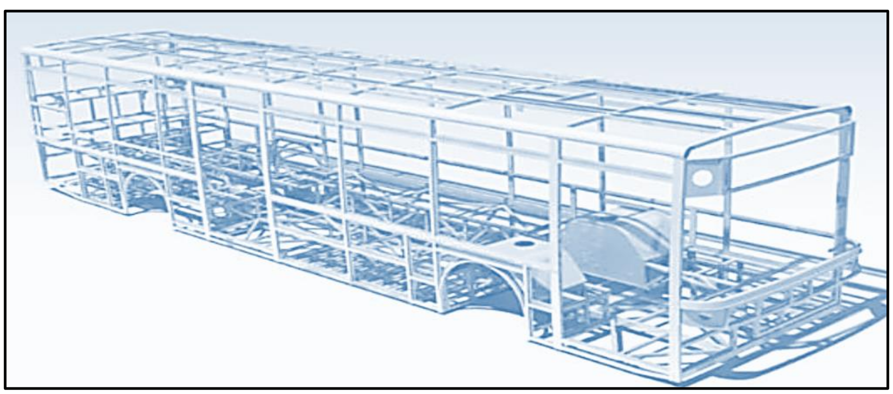

Figure 1.12 Bus body structure

Heat input and loss are greatly affected by design and glass. Buses differ from motor vehicles not only in size and handling but also in their design (BOLTZ, 2011, p. 37).

In the case under study, the bus possesses 25 passenger chairs, besides, 26 passengers can travel standing.

1.4 Bus body insulation materials

Materials that insulate sound and heat are inserted into the spaces between the outside and inner lining. Additionally, the coaches' side windows have double glazing. Below different insulation materials for different bus compartments have been shown (Mezarciöz, 2015)

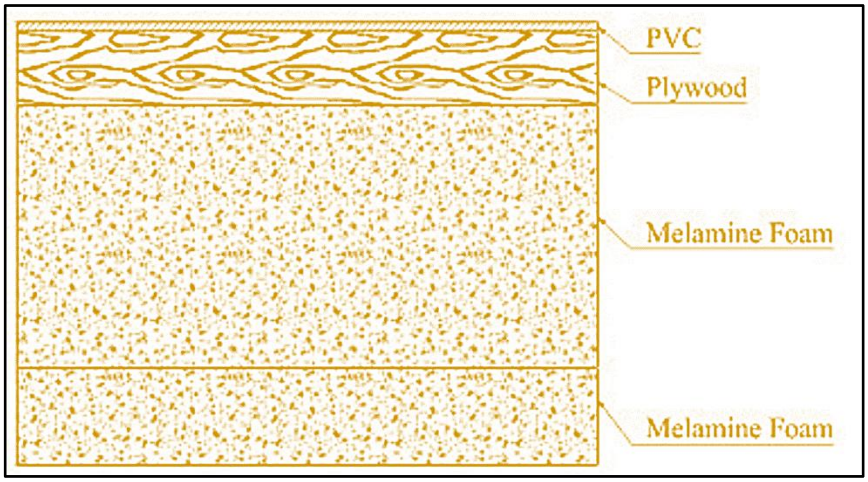

Figure 1.13 Insulation material used in engine room

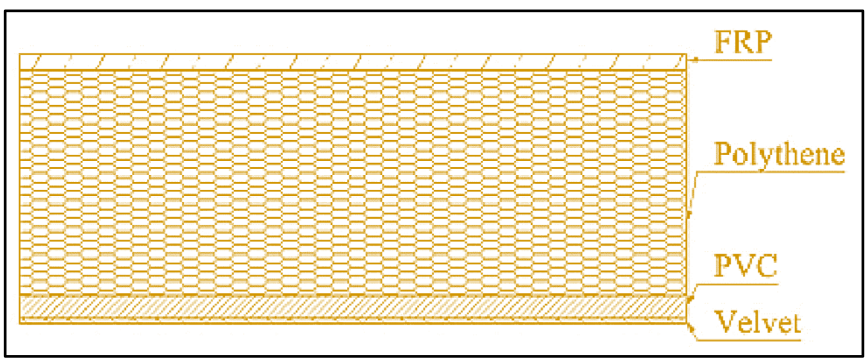

Figure 1.14 Insulation material used on roof structure

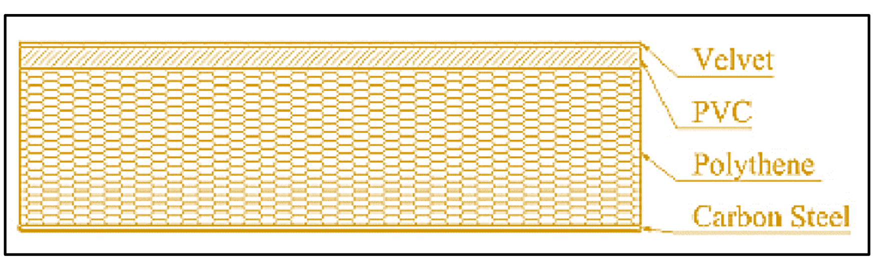

Figure 1.15 Insulation material used on side body

1.5 Computational Fluid Dynamics

Computational fluid dynamics (CFD) is a branch of fluid mechanics that implements numerical analysis and data structures to analyze fluid flows. It is based on mass, momentum, and energy conservation laws governing fluid motions. For the simulation of free-steam flows of fluid and its interaction with solid surfaces, computers are used. Depending on the complexity of a problem usage of supercomputers might be required. Application areas of Computational Fluid Dynamics range from fluid flow, heat transfer, aerodynamics, weather simulation, environmental engineering, system design and analysis, and biological engineering to visual effects for games (Sodja, 2007).

Computational fluid dynamics has become a known tool in design and performance analysis, however, one of the main challenges of CFD is the determination of a suitable turbulent model. There are several turbulence models available (Neel, 1997). In the current study k-ϵ, Standart, and k-ω SST turbulence methods are used to analyze flow in our domain. In the end, the numerical results are compared with the experimental ones.

CFD analyses are based on Discretization methods. Discretization methods are used to divide a continuous function into discrete functions, where the solution values are defined at each point in space and time (Sodja, 2007). Ansys program uses the Finite Volume method in which values are defined at node central points. With the finite volume method, we are representing and evaluating the partial differential equations in the form of algebraic equations. In the finite value method with the help of the divergence theorem, volume integrals in partial differential equations containing divergence terms are converted to surface integrals.

Another aspect that is a serious matter is the generation of mesh. When solving a CFD problem generation of mesh with a finite number of elements is a part of the process. The number of mesh elements must be increased up to a point where no difference in study results occurs, that is, our results become independent of mesh element size (Anderson, 1995). In our study, 3 different meshes with different element sizes will be used to accomplish mesh independency.

After finishing the generation of mesh and determining of proper turbulence model, the air channel performance will be examined.

1.5.1 History of evolution of CFD

The first calculations resembling modern CFD were done by Lewis Fry Richardson. In these calculations, he divided a physical domain into cells using finite differences. Despite the fact that his attempts ended in failure, these calculations set the basis for modern CFD analysis.

With the evolution of computers implementation of CFD analysis become valid for users. In 1957, at Los Alamos National Lab, the group T3 first time in history used computers for modeling fluid flow.

In 1967 John Hess published their first paper with a 3D model of fluid flow. His discretization method was discretizing surfaces by panels. However, this method was simplified and didn't include lifting flows, therefore, was mainly applied to aircraft fuselages and ship hulls. The first lifting Panel Code was described by Paul Rubbert and Gary Saaris of Boeing Aircraft in 1968.

Before the development of Full Potential codes, there was another type of code that were using Transonic Small Disturbance equations. Especially, 3D WIBCO code, developed by Charlie Boppe of Grumman Aircraft in the 1980s, has been widely used.

The weakness of the panel method was based on the fact that they were not capable of solving non-linear flow present at transonic speeds. In 1970, Earll Murman and Julian Cole published a description of the usage of Full Potential equations. Frances Bauer, Paul Garabedian, and David Korn of the Courant Institute at New York University (NYU) wrote a series of two-dimensional Full Potential airfoil codes that were widely used. Antony Jameson worked with David Caughey to develop the important three-dimensional Full Potential code FLO22 in 1975.

The next stage was the generation of Euler equations through which more accurate solutions could be reached. The first time it was applied by Jameson in his 3D FLO57 code. On the basis of this code, there have been created several programs such as Lockheed's TEAM program and IAI/Analytical Methods' MGAERO program.

In all the cases the final target of all developers was the Navier-Stokes equations. First, the code using the method was NASA Ames' ARC2D. Afterward, lots of 3D codes were developed leading to numerous commercial packages (Jens-Dominik Mueller, Essentials of Computational Fluid Dynamics).

1.5.2 Navier-Stokes equations

The fundamental basis of almost all CFD problems is the Navier–Stokes equations, which define many single-phase fluid flows. Generally, a problem is composed of four unknowns: u, v, and w are sped in x, y, and z directions, and P is pressure. To account for compressibility of flow and heat transfer cases energy equation is also being added to the set of equations. To be more precise, for heat transfer and compressibility case temperature and density are added accordingly. To conclude, in the case of compressible flow we have 5 equations: Continuity, X-momentum, Y-momentum, Z-momentum, and Energy equation.

For determination of the origins of the shown equations, we must refer to mass conservation and momentum equations defined for the Lagrange method. As it is known, the Eulerian approach is more practical for fluid mechanics applications, therefore, the Reynolds Transfer theorem is being used for the generation of a bridge between Lagrangian and Eulerian equations. The general form of the Reynolds Transfer theorem is shown below. (Cengel and Cimbala's Fluid Mechanics)

$$\frac{DB_{sys}}{Dt} = \frac{\partial}{\partial t}\int_{CV} \rho\, b d\forall \, + \int_{CS} \rho\, bV \cdot ndA$$

According to the Lagrangian system notion of mass, neither can enter nor leave a system. Therefore, dm/dt=0. If the Reynold transfer theorem is applied to this formulation, for control volume we will get the following equations.

$$B = bm \;\rightarrow b = 1.$$

$$\frac{Dm_{sys}}{Dt} = \frac{\partial}{\partial t}\int_{CV} \rho\, d\forall \, + \int_{CS} \rho\, V \cdot ndA \, = \, 0$$

This expression is written for constant control volume with doesn't move and deform. Therefore, the integral's limit values also will be constant which will result in taking the partial derivative with respect to time into the integral term.

$$\int_{CV} \frac{\partial\rho}{\partial t} d\forall \, + \int_{CS} \rho\, V \cdot ndA \, = \, 0$$

Another point of confusion is related to the limits of integration is that the first term is being defined over volume, while the second term over the surface. To bring both integrals to the same level, Gauss's Divergence Theorem must be applied. The general form of the theorem is shown below. (Cengel and Cimbala's Fluid Mechanics)

$$\int_{\forall} \vec{\nabla} G d\forall = \int_{A} G \cdot ndA$$

$$(G = \rho V) \rightarrow \int_{CV} \frac{\partial\rho}{\partial t} d\forall \, + \int_{CV} \vec{\nabla}\rho\, V d\forall = \, 0$$

This simplification allows us to sum both expressions inside a single integral. If integral over a volume equals zero, it means its internal part is also equal to zero.

$$\int_{CV} \left[\frac{\partial \rho}{\partial t} d\forall + \vec{\nabla} \rho V d\forall\right] d\forall = 0$$

Lastly, we get the Conservative form of the Continuity equation which is used in CFD codes.

$$\frac{\partial \rho}{\partial t} d\forall + \vec{\nabla} \rho V d\forall = 0$$

Following similar steps, we can also obtain Cauchy equations which with some simplifications lead to Navier-Stokes equations. First, we start with a modified form of Newton's second law.

$$F = ma = \frac{dmV}{dt}$$

If the summation of applied forces is equal to zero, the expression shown with deviation with respect to time also must be equal to zero, which means the terms mV = 0. This expression is called the Linear Momentum expression.

$$\sum F = \frac{dmV}{dt} = 0 \rightarrow mV = 0$$

As a second step, the Reynolds Transport theorem must be applied for further development of the equations.

$$B = bm \rightarrow b = V.$$

$$\frac{D(m\overrightarrow{V})_{sys}}{Dt} = \frac{\partial}{\partial t} \int_{CV} \rho \vec{V} d\forall + \int_{CS} \rho \vec{V}\vec{V} \cdot n dA = \sum F_{CV} = F_{weight} + F_{surface} + F_{other}$$

Weight forces are composed of several forces, such as gravitational force, electromagnetic force, and so on. As in our problem at hand, there is no effect of electromagnetic forces, we won't give detailed information about it. If we examine the gravitational force acting on an infinitesimally small piece of volume, it can be written in the shown form.

$$F_{weight} = \int_{CV} \rho \vec{g} d\forall$$

Surface forces fall into two groups, a) pressure forces and b) viscose forces. Besides, viscous forces are also grouped as viscose normal and viscose share forces. For accommodation of presence of viscose forces, they all can be gathered into the Stress tensor, σij.

$$F_{surface} = \int_{CS} \sigma_{ij} \cdot \vec{n} dA$$

With the application of the Divergence theorem, we can again turn the parts of the equation referring to integration over the surface to integration over volume.

$$\int_{CS} \rho \vec{V}\vec{V} \cdot n dA = \int_{CV} \vec{\nabla}\rho\vec{V}\vec{V} d\forall$$

$$\int_{CS} \sigma_{ij} \cdot \vec{n} dA = \int_{CV} \vec{\nabla}\sigma_{ij} d\forall$$

$$\frac{\partial}{\partial t}\int_{CV} \rho \vec{V} d\forall + \int_{CV} \vec{\nabla}\rho\vec{V}\vec{V} d\forall = \int_{CV} \vec{\nabla}\sigma_{ij} d\forall + \int_{CV} \rho\vec{g} d\forall$$

As mentioned previously, as our Control volume is conservative, that is, doesn't move and deform, we can take the partial derivation inside the integral and take integral over all terms and equal to zero. After performing the mentioned steps, we obtain the Cauchy equation.

$$\frac{\partial\rho\vec{V}}{\partial t} + \vec{\nabla}\rho\vec{V}\vec{V} = \vec{\nabla}\sigma_{ij} + \rho\vec{g}$$

For a Cartesian coordinate system, this equation is composed of three parts. An additional term that also comes into play is the Continuity equation that we have defined above. Normally, if we accept the density to be constant, we have four unknown terms, Pressure, and 3 components of speed for each coordinate direction, u, v, and w. Under these conditions, we can find the shown 4 unknown terms using 4 equations. But the presence of a stress tensor brings about 6 unknown stress expressions which we must link to the unknown terms for decreasing the number of unknowns and make the expressions solvable again.

$$\sigma_{ij} = \begin{bmatrix} \sigma_{xx} & \sigma_{xy} & \sigma_{xz} \\ \sigma_{yx} & \sigma_{yy} & \sigma_{yz} \\ \sigma_{zx} & \sigma_{zy} & \sigma_{zz} \end{bmatrix} = \begin{bmatrix} -P & 0 & 0 \\ 0 & -P & 0 \\ 0 & 0 & -P \end{bmatrix} + \begin{bmatrix} \tau_{xx} & \tau_{xy} & \tau_{xz} \\ \tau_{yx} & \tau_{yy} & \tau_{yz} \\ \tau_{zx} & \tau_{zy} & \tau_{zz} \end{bmatrix}$$

As this is a symmetric matrix, the number of unknown terms is six. For linking the stress expressions with speed and pressures we must use Structural equations. For solid bodies, the shown expression links stress to strain rate, $\sigma_{ij} = E\varepsilon_{ij}$. For the Newtonian type of fluids, this expression can be written as $\tau_{ij} = 2\mu\varepsilon_{ij}$.

$$\sigma_{ij} = \begin{bmatrix} -P & 0 & 0 \\ 0 & -P & 0 \\ 0 & 0 & -P \end{bmatrix} + 2\mu \begin{bmatrix} \varepsilon_{xx} & \varepsilon_{xy} & \varepsilon_{xz} \\ \varepsilon_{yx} & \varepsilon_{yy} & \varepsilon_{yz} \\ \varepsilon_{zx} & \varepsilon_{zy} & \varepsilon_{zz} \end{bmatrix} = \begin{bmatrix} -P & 0 & 0 \\ 0 & -P & 0 \\ 0 & 0 & -P \end{bmatrix} +$$

$$+ 2\mu \begin{bmatrix} \frac{\partial u}{\partial x} & \frac{1}{2}\left(\frac{\partial u}{\partial y} + \frac{\partial v}{\partial x}\right) & \frac{1}{2}\left(\frac{\partial u}{\partial z} + \frac{\partial w}{\partial x}\right) \\ - & \frac{\partial v}{\partial y} & \frac{1}{2}\left(\frac{\partial v}{\partial z} + \frac{\partial w}{\partial y}\right) \\ - & - & \frac{\partial w}{\partial z} \end{bmatrix}$$

After the shown acceptance, we can relate our stress expressions to pressure and speed components which will bring down the number of unknowns to four.

$$\sigma_{xx} = -P + 2\mu\frac{\partial u}{\partial x} \qquad \sigma_{xy} = \mu\left(\frac{\partial u}{\partial y} + \frac{\partial v}{\partial x}\right) = \sigma_{yx}$$

$$\sigma_{yy} = -P + 2\mu\frac{\partial v}{\partial y} \qquad \sigma_{xz} = \mu\left(\frac{\partial u}{\partial z} + \frac{\partial w}{\partial x}\right) = \sigma_{zx}$$

$$\sigma_{zz} = -P + 2\mu\frac{\partial w}{\partial z} \qquad \sigma_{yz} = \mu\left(\frac{\partial v}{\partial z} + \frac{\partial w}{\partial y}\right) = \sigma_{zy}$$

However, in front of expression of stress, we have the Gradient operator which is $\vec{\nabla} = \left[\frac{\partial}{\partial x} + \frac{\partial}{\partial y} + \frac{\partial}{\partial z}\right]$. Having the information shown, the terms can be further adjusted to reach a most useful form of expression.

$$\vec{\nabla}\sigma_{ij} = \begin{bmatrix} \frac{\partial \sigma_{xx}}{\partial x} & \frac{\partial \sigma_{yx}}{\partial y} & \frac{\partial \sigma_{zx}}{\partial z} \\ \frac{\partial \sigma_{xy}}{\partial x} & \frac{\partial \sigma_{yy}}{\partial y} & \frac{\partial \sigma_{zy}}{\partial z} \\ \frac{\partial \sigma_{xz}}{\partial x} & \frac{\partial \sigma_{yz}}{\partial y} & \frac{\partial \sigma_{zz}}{\partial z} \end{bmatrix}$$

Each term can be written in the open form correspondingly.

$$\frac{\partial \sigma_{xx}}{\partial x} = \frac{\partial}{\partial x}\left[-P + 2\mu \frac{\partial u}{\partial x}\right] \rightarrow P = cons. \rightarrow \frac{\partial \sigma_{xx}}{\partial x} = -\frac{\partial P}{\partial x} + 2\mu \frac{\partial^2 u}{\partial x^2}$$

Then for the x component of coordinates, the Cauchy expression can be written as follows. Here application of the Laplace operator makes equations look compact. The general form of the Laplace operator is $\nabla^2 = \frac{\partial^2}{\partial x^2} + \frac{\partial^2}{\partial y^2} + \frac{\partial^2}{\partial z^2}$.

$$\frac{\partial \rho \vec{V}}{\partial t} + \vec{\nabla} \rho \vec{V} \vec{V} = -\frac{\partial P}{\partial x} + \rho g_x + \mu \left[\frac{\partial^2 u}{\partial x^2} + \frac{\partial^2 u}{\partial y^2} + \frac{\partial^2 u}{\partial z^2}\right] = -\frac{\partial P}{\partial x} + \rho g_x + \mu \nabla^2 u$$

Finally, we reach the compact form of the Navier-Stokes equation.

$$x: \frac{\partial \rho u}{\partial t} + \vec{\nabla} \rho u u = -\frac{\partial P}{\partial x} + \rho g_x + \mu \nabla^2 u$$
$$y: \frac{\partial \rho v}{\partial t} + \vec{\nabla} \rho v v = -\frac{\partial P}{\partial y} + \rho g_y + \mu \nabla^2 v$$
$$z: \frac{\partial \rho w}{\partial t} + \vec{\nabla} \rho w w = -\frac{\partial P}{\partial z} + \rho g_w + \mu \nabla^2 w$$
$$General\ form: \frac{\partial \rho \vec{V}}{\partial t} + \vec{\nabla} \rho \vec{V} \vec{V} = -\vec{\nabla} P + \rho \vec{g} + \mu \nabla^2 \vec{V}$$

The important difficulties related to the equation come from the following terms:

1) $\frac{\partial \rho \vec{V}}{\partial t}$ – makes the equation related to time.

2) $\vec{\nabla} \rho \vec{V} \vec{V}$– makes the equation non-linear.

3) $-\vec{\nabla} P + \rho \vec{g}$– make the equation non-homogeneous.

4) $\mu \nabla^2 \vec{V}$ – contains terms from second derivation level.

For Laminar flow, the direct form of these expressions is being used. Nonetheless, for turbulent flow different turbulent models are defined which have various usage areas.

Chapter 2

Literature survey

In this chapter studies about mobile air conditioning systems alongside CFD applications in similar fields are examined. Especially, CFD analysis in automotive industries and HVAC (Heating, Ventilation, and Air conditioning) studies are investigated.

2.1 Studies on Automotive HVAC Systems

In his thesis, Karasu (2022) looked at the air and temperature distribution within a bus. As a starting step, one validation article has been chosen to validate the analysis. The chosen article includes experimental findings so that analytical findings and experimental findings may be contrasted. Starting from this point, the 3D design application was used to generate the flow volume of the bus, which has been given cross-sectional geometry. The procedure of creating geometry, as described in the article, overlooked the smooth distribution of the flow and components such tiny indentations and protrusions that would impair convergence.

Barut (2018) obtained and compared the temperature distribution in the bus cabin using both experimental and numerical methods. In most HVAC studies CFD package program was used as it is. In order to give reasonable initial values to the analysis, the experimental environment was created as the entire bus. The time-dependent temperature results obtained at certain locations were compared with the results from the analysis. While creating the experimental environment, the outdoor temperature was fixed at 45°C and the cabin temperature was fixed at 24°C, which is suitable for thermal comfort. For the analysis $k - \epsilon\ Standart$ method have been used.

Ekici and Güney (2016), who examined the air flow and temperature distribution in the bus cabin with both numerical and experimental methods. In the model, the 3D cabin model was set up and the results in a seat row were examined. A tetrahedral mesh structure is used to capture the air flow movement in the cabin in detail. In addition, a prismatic layered mesh structure has been applied to the walls, seats and heaters. During the numerical solution, the quadratic discretization and SIMPLE algorithm was applied to the pressure velocity couple for the convection terms.

Ahmad Shafie (2015) examined the weather and temperature results in a small section of the coach in this article. In the analyzes made for two different cases, the effect was observed by changing the speed of the air coming out of the ventilation hole. The weather and temperature boundary conditions were determined by the data from the experimental results. The $k - \varepsilon$ turbulence model, which can capture the indoor air distribution at a high rate, was preferred in the analyses. Fast convergence in three-dimensional analysis Tetrahedron elements are used in the network structure because it can provide In order to show the independence from the mesh structure, the temperature of the air was measured according to different mesh numbers. When the results are examined, it is observed that if the speed of the air feeding the indoor environment is 3.1 m/sec, the air temperature above and below the seat decreases by 0.3 ℃.

Mansour et al. (2007) introduced a unique control technique for a new rooftop bus multiple-circuit AC system working under partial load situations in order to increase energy efficiency and passengers' thermal comfort. A novel energy-saving method for bus air conditioning in tropical regions was introduced as a result of the study. Particularly under low sensible load situations with compressor cycling rates not surpassing 4 cycles/hour, the designed system was able to provide appropriate thermal comfort in the bus passenger compartment. The innovative technique was dependent on an automated controller being given an accurate representation of the cooling demand in terms of temperature differential.

Qi et. al. (2007), performed an experimental study of an auto-controlled mobile AC system with an externally controlled variable displacement compressor. A new displacement of externally controlled variable displacement compressor was developed for evaporator characteristics and in-car temperature fluctuations. Wind tunnel results showed that a MAC system with an externally controlled variable displacement compressor can maintain the derivation of in-car temperature conditions no more than 2°C in comparison with the user's desired one. The advantage of the MAC system is that it gives the occupants good thermal comfort in rapidly changing environmental conditions. The made comparison between externally controlled variable displacement compressor and fixed displacement compressors have shown that the discharge pressure of externally controlled variable displacement compressor is faster and its effect is seen in internal climate changes.

Kaynaklı and Horuz (2003), in their study, examined automotive air conditioning systems. The performance of the system was investigated under different conditions of ambient temperature, evaporator, condenser, and compressor speeds. Refrigerant mass flow rate, compressor power consumption, COP value, and cooling load were examined and optimum operating conditions were determined.

An experimental AC test rig for a full-scale bus was conducted by Conceicao et. al. (1997). He characterized the conditioned air flow around passengers and analyzed the thermal comfort conditions perceived by passengers. This study also embraces the evaluation of indoor air quality and exchange rate in the passenger compartment of an intercity bus.

2.2 Studies on Underhood Thermal management and Thermal Comfort

Babu, R., Kumar, V (2022) investigated the underhood thermal management of the newly introduced electric tractor, with the target of managing the heat generated out from the major heat contributing sources. The alignment of the fan with some design modifications has been made on the basis of CFD simulation. For this work, a RANS method utilizing the k-Ɛ turbulence model has been implemented in the commercial CFD solver STAR-CCM+.

Çağlayan (2021) studied thermal underhood analysis of a heavy commercial vehicle using open Source CFD Package OpenFOAM. Surface-to-surface radiation has been used to simulate the radiation heat transfer in the underhood region. With differences under 100C, the turbocharger heat shield temperature predicted by the solver matches the observations pretty well.

Wang, Yan (2016) study applied 1D/3D collaborative computing simulation method for vehicle thermal management. They analyzed the influence of the thermodynamic systems and the engine compartment geometry on the vehicle performance providing the basis for the matching energy consumptions of thermodynamic systems in the underhood.

Wu and Ahmed (2012) investigated a unique method of air supply that might enhance ventilation efficiency without raising the pace of the fresh air supply. Due to the necessity of aircraft cabin ventilation for commercial passenger flights, effective fresh air delivery has emerged as a significant research concern in the HVAC industry.

Büyükalaca et al. (2011) employed the "Radiant Time Series" approach to calculating the cooling load of a bus since there isn't a generally acknowledged calculation procedure for the analysis of the cooling load of non-stationary volumes with a lot of variable characteristics, like buses.

Zgören et al. (2011) evaluated the hourly dynamic cooling load capacity (heat gain) of a sample building using the radiant time series (RTS) approach and meteorological data from the years 1997 to 2008, including solar radiation, outside air temperature, and wind speed.

In their investigation, Ekeroth and Martinsson (2011) concentrated on the numerical simulation of a large truck driving uphill at a speed of 30 km/h.

In Sevilgen's (2010) study, the distribution of temperature and airflow in the car's cabin was numerically analyzed in three dimensions using the Computational Fluid Dynamics method. In order to accomplish this, a three-dimensional car cabin featuring windows and outside surfaces was designed using the actual measurements of a car. A virtual manikin divided into 17 pieces with real measurements and physical shape was incorporated into the model of the car interior in order to evaluate the results of the numerical analysis according to thermal comfort.

The main goal of the study by Khaled et al. (2009) was to redesign the under hood architecture in order to lessen the aero thermal cooling drag and, as a result, the cooling airflow rate in the under hood component.

Mui and Wong (2007) looked at office occupant load characteristics, an example weather year, and energy performance and consumption. The study looked at the applicability of the current example weather year and changes in occupant load. In order to satisfy the requirement of occupant loads and current outdoor information, the developed methodologies would be helpful for an efficient design and an accurate cooling load computation of air-conditioned buildings.

In their investigation, Fournier and Digges (2004) examined four distinct car models at hood temperatures. 11 thermocouples were mounted in 4 distinct vehicles' underhood for their investigation, and measurements were taken in 3 different test scenarios: standing still, traveling at a constant pace, and climbing a hill.

Körbaht's (1999) analysis of the factors influencing the heating condition in buses. The intercity buses outside the shell's heat dispersion as well as its inside temperature were determined under specific circumstances.

2.3 CFD Studies

Valiyev (2021) in his study, examined the HVAC of two different busses with a length of 12m and standing and sitting passenger capacities of 25 and 62 respectively. CFD studies of air channels were made using SolidWorks CAD software. In the analysis, the ambient temperature of the inner bus region was tried to be decreased from 30 to 16C.

Esen (2018) within the scope of the thesis study, studied computational fluid mechanics and natural ventilation analysis of wind trap and exhaust chimney geometries of a single-storey 18 m x 14.5 m x 4 m building. A 5.5 m high wind trap is placed on this building. One shot behind the wind trap chimney is positioned.

Mezarciöz (2015) in his study examined the design of an air channel for intercity busses with a capacity of 50 passengers. In the design, he compared 5 different turbulence models, k-ε Standard, k-ε Realizable, k-ε RNG, k-Ω Standard, Spallart-Almaras.

In a military ground vehicle design process, Bayraktar (2012) created 1-D and 3-D unsteady CFD-based simulation tools. On a computer cluster, numerous operating scenarios for the HVAC and powertrain cooling systems were simulated using a variety of fidelity tools. Even though 1-D simulation tools are useful for making initial predictions about a developed framework, it has been shown that higher fidelity 3-D CFD calculations and occasionally climatic testing are needed for examining the transient behavior of a vehicle thermal system.

With six alternative air leak geometries positioned appropriately on its perimeter, Moujaes and Gundavelli (2012) employed a three-dimensional computational fluid dynamics model to simulate fluid flow in a duct and its simulated leaks. This was accomplished by using the $k - \epsilon$ turbulence model for high Reynolds number flows and varying the Reynolds numbers to mimic various flow conditions.

In his paper, Sardar (2010) examined the three-dimensional simulation analysis of a diesel engine utilizing a moving dynamic mesh with several combustions and turbulence models, including $k - \epsilon$ and $k - \omega$.

A numerical analysis of a turbulent, recirculating, two-dimensional flow within a passenger automobile cabin using the $k - \epsilon$ turbulence model was given by Jalil and

Alwan in 2007. To demonstrate their effects on the flow field and temperature distribution inside the automobile cabin, many characteristics were considered. These characteristics included the quantity and position of the air conditioning system's inlets inside the car's interior, various air temperatures and velocities at the inlets, as well as various diffuse solar radiation and solar daytime intensity.

The appropriateness of various turbulence models in the intricate swirling flows that occur in tangential inflow cyclones was examined by Kaya and Karagoz in 2007. Under certain boundary conditions, the numerical solution of the 3D stable governing equations for the incompressible, turbulent flow inside the cyclone was performed using the Fluent CFD code.

Zyl (2006) did an experiment utilizing computational fluid dynamics (CFD) to numerically analyze the flow and heat processes occurring in a passenger car's undercarriage.

Huang and Han (2002) used simulations of the soak and cool down of a passenger compartment to show the capabilities of CFD analysis. The success of Virtual Thermal Comfort Engineering depended heavily on forecasts of precise airflow velocity and temperature distributions. The present transient simulation can more precisely forecast air temperatures surrounding an individual in the passenger compartment than thermocouple observations can in most cases.

Chapter 3

CFD analysis of the air channel

In this chapter study of the air channel through Computational Fluid Dynamics is performed and the outcome was put in comparison with experimental results. In the analysis error elimination method and application of $\boldsymbol{k-\epsilon\ Standart}$ and $\boldsymbol{k-\omega\ SST}$ methods are applied.

3.1 3D shape of air channel

In the thesis application, the right-side air channel of a bus has been used. Below we have several photos of the project from different perspectives. In the air channels, the main used material is ABS which is used in wall and outlet sections. However, the skeleton of the structure lies on aluminum profiles.

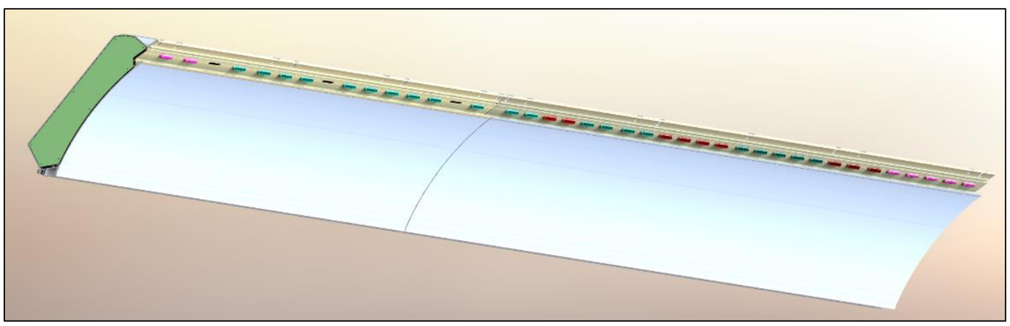

Figure 3.1 Perspective view of the air channel

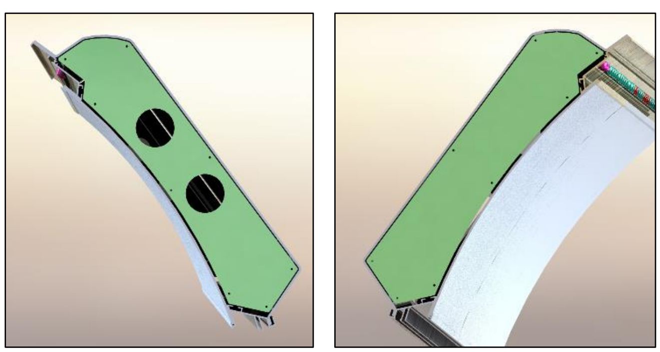

Figure 3.2 Rare view of the air channel

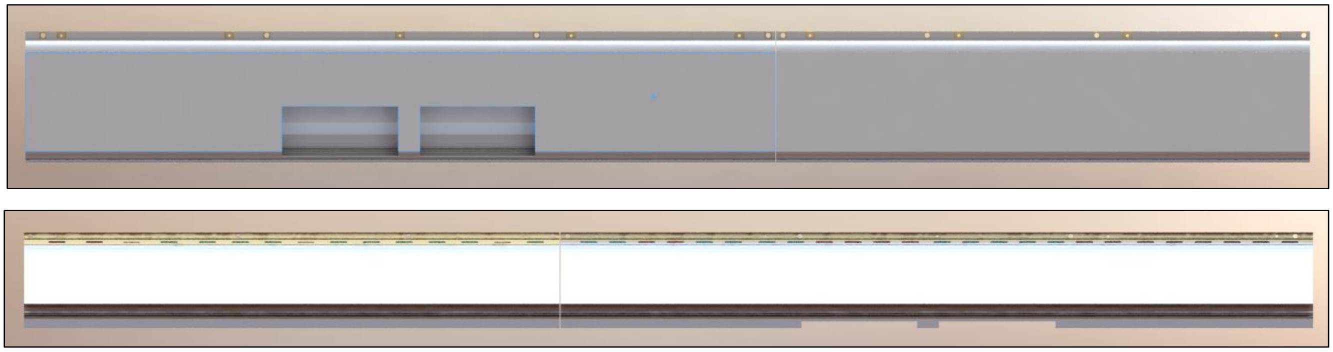

Figure 3.3 Top and bottom sections views of the air channel

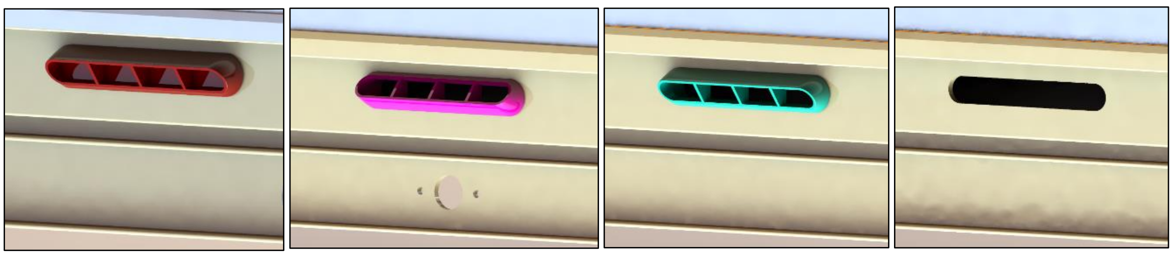

Figure 3.4 Different outlet sections of the air channel

In this photo, we have the discharge parts of the air channels. The red ones are closed, purple and green ones are open, however, they are oriented in different directions. The last gap is used for assembly purposes and isn’t an air discharge port. In the study, the purple and green ports, for the purpose of simplification, are positioned in the same direction.

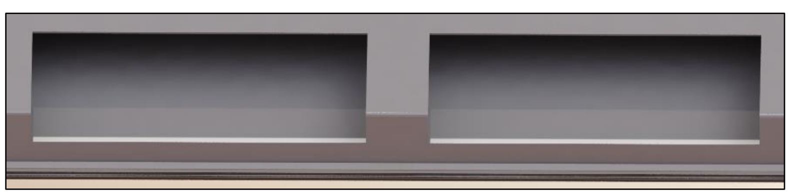

Figure 3.5 Inlet sections of the air channel

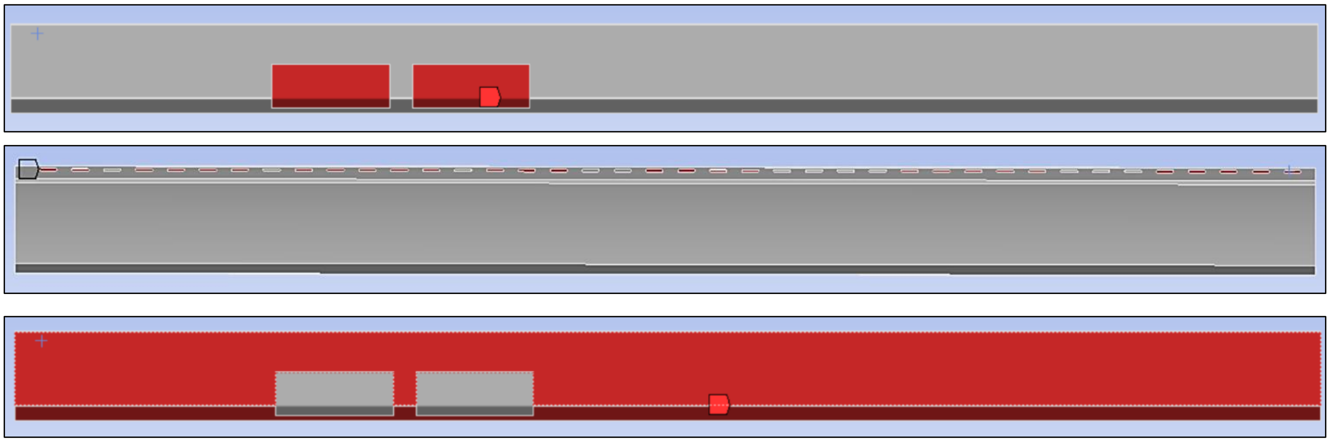

Figure 3.6 Inlet, out and wall boundary conditions of the air channel

3.2 Problem definition

The project investigates the efficiency of a bus cooling channel. For the determination of investigated outlet velocity of channels, for a mesh made of an infinite number of cells, an extrapolation method is used. However, for its application three different mesh sizes, that is, fine, medium, and course meshes are examined and with appropriate methods suggested by the literature applied. These three meshes are also used for the study of mesh independency.

Besides, two turbulent models, k-ε and k-ω, will be used and a comparison between models will be done.

3.3 Determination of flow type

3.3.1 Determination of Reynold value

3.3.1.1 Determination of Reynold value for channel

Most kinds of fluid flow are turbulent. However, to define it we need Reynolds value. The general formulation of Reynold's value is indicated below:

$$Re = \frac{\rho V D_h}{\mu}$$

Here, ρ- is the density of the fluid (for air at 15°C is 1.225 kg/m3), V-is the speed of the fluid (1.1 m/s), Dh-is the hydraulic diameter, and μ is the dynamic viscosity of fluid (for air at 15°C is 1.81x10^{-5} kg/m·s). First, we must define hydraulic diameter which is defined with the following expression:

$$D_h = \frac{4A_c}{P}$$

Here Ac is the area of the channel in which we have fluid flowing and P is the perimeter of the region which is in contact with the fluid. Both values are defined with the help of the program. Area and perimeter are defined are 36579.3832mm² = 0.036579383m² and 1021.1601mm = 1.0211601m accordingly. Thus, D_h is 0.1432856m.

Replacing all the values we define the Reynold's value as 8433.75. In viscose internal flows, laminar, transient and turbulent flows are categorized according to the following values: Re≤2300 – laminar flow, 2300 <Re<4000 – transient flow, and Re>4000 turbulent flow. We can conclude that the case under investigation falls into the group of turbulent flow.

3.3.1.2 Determination of Reynold value for outlet section

For the outlet section, the area and perimeter are 688.54mm² and 153.42mm correspondingly. From the given values we can calculate the Dh value: 0.017952.

The average speed at the outlet section is 2.6m/s. Afterward, the Reynold value is defined for the outlet section: 3258.96 which falls into the transient flow region.

3.4 Mesh application process

After retrieving the shape of our air channel, we start the meshing process. For this purpose, we use the Fluid module of the Ansys program. Ansys CFX and Ansys Fluent, one of the famous commercial CFD software packages, is based on a finite volume method approach. The finite volume method (FVM) is a discretization technique for partial differential equations, especially those that arise from physical conservation laws. FVM uses a volume integral formulation of the problem with a finite partitioning set of volumes to discretize the equations. In FVM the computation takes place at cell centers and the values are linked linearly.

As the inner part of the channel is composed of comparatively complex shapes and sharp edges, according to the suggestion of the Ansys manual, the best meshing element which would meet our needs is tetrahedrons. In all three cases, the application of the inflation layer wasn't feasible due to the complexity of geometry. Besides the application of inflation layers was decreasing Skewness and Orthogonality qualities, which in its turn brought undesired outcomes. However, the software itself uses wall functions for better capture of non-linear behaviors of fluids at contact regions with walls of solid bodies. As mesh size on surface regions was quite small and hardware wasn't capable of dealing with small mesh size, further betterment was done by the software through the application of wall function which relies on changing the values of kinematic viscosity and heat diffusivity.

3.4.1 Mesh Quality

In CFD analysis three most important mesh qualities are Aspect ratio, Skewness, and Orthogonal Quality. According to the literature, to achieve a desirable outcome with a lower risk of deviation from real results and a long solution process, the mentioned parameters must fall within the shown limits. (ANSYS Fluent User's Guide). Below represented values, that is, aspect ratio, skewness, and non-orthogonality qualities are illustrated for fine mesh.

3.4.1.1 Definition of Aspect rate

The first of these values is the Aspect ratio. It is defined as the ratio between long and short parts of our cell geometry.

$$Aspect\ ratio\ = \frac{L}{S}$$

For a square cell, its value is 1. Normally, we want its value to be around 1, however, up to 10, this value still brings about desired results. To improve the shape of the cells, it is useful to have quantitative metrics that can be used to assess how close the cells are to perfect shapes. When the aspect ratio for a particular cell reaches very high values, then its area increases compared to other cells. In return, this face dominates the contribution of other cells. As a result, we get instability in the system of equations.

The aspect ratio is defined in different ways in different programs. In Ansys Fluent, the distance from the cell center to corner points and middle points of faces is being evaluated. Afterward, the ratio between longest and shortest distances is defined as an aspect ratio. However, through this method, we can't achieve the value of 1 for a perfect square shape. Nevertheless, small deviations from the perfect value, 1, are acceptable.

3.4.1.2 Definition of Skewness

Skewness is the deviation of elements' shape. It is about the departure of a face shape from its regular shape. As an example, we can examine the shown triangles.

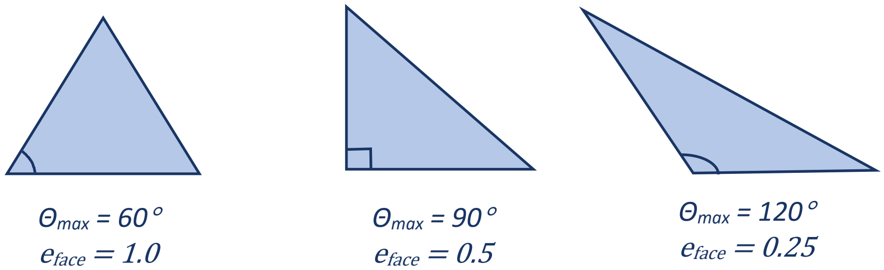

Figure 3.7 Illustration of skewness property of cells

The first triangle on the left side possesses the perfect shape having all internal angles equal to 60 degrees. However, going towards the left-hand side, the shape triangles depart from their perfect shape and generate skewed cells. Skewness is the property that defines this deviation. To define the equiangular skewness the following formulation is used:

$$e_{face} = max\left[\frac{\theta_{max} - \theta_e}{180° - \theta_e}.\frac{\theta_e - \theta_{min}}{\theta_e}\right]$$

Here where θmin and θmax are the maximum and minimum corner angles on the face. After determination of e_{face} for each cell, the highest equiangular skewness is taken as the e_{cell}:

$$e_{cell} = max(e_{face,1}, e_{face,2}, e_{face,3}, \dots e_{face,n})$$

Below, on the graph, we have the range of values of skewness between 0 and 1 and their acceptance level.

Excellent	Very good	Good	Acceptable	Bad	Unacceptable
0-0.25	0.25-0.5	0.5-0.8	0.8-0.94	0.95-0.97	0.98-1.00

Table 3.1 Skewness quality values

3.4.1.3 Definition of Orthogonality

Non-orthogonality is the metric that directly affects CFD stability. To understand the concept behind orthogonality, let's examine the photo shown below. Here we have two cells in contact, triangle and skewed quadrilateral. Central points of cells are connected with the d_{AB} vector and the vector normal to the surface of the triangle isn't parallel with the direction of d_{AB}.

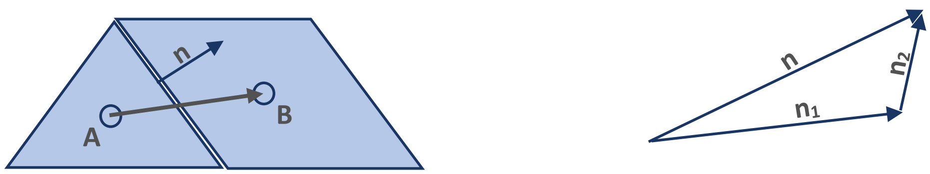

Figure 3.8 Illustration of orthogonality property of cells

Non-orthogonality is the angle between the surface normal angle and the d_{AB} vector. First, we define the scalar multiplication of indicated vectors.

$$d_{AB} \cdot n = |d_{AB}||n|cos(\theta_{face})$$

$$\theta_{face} = cos^{-1}\left[\frac{d_{AB} \cdot n}{|d_{AB}||n|}\right]$$

As an indication of perfect quality, we can look at the case of $\theta_{face} = 0°$. Conversely, an angle greater than 90° indicates that the face is collapsed. To have the non-orthogonality angle equal to zero, we should have two perfectly neighboring quadrilaterals.

After the calculation of face non-orthogonality, cell orthogonality is defined as the highest of these values.

$$\theta_{cell} = max(\theta_{face,1}, \theta_{face,2}, \theta_{face,3}, \ldots \theta_{face,n})$$

However, non-orthogonality quality, which is a value between 0 and 1, is defined through the normalization of the cell value.

$$\theta_{quality} = 1 - \frac{max(\theta_{face,1}, \theta_{face,2}, \theta_{face,3}, \ldots \theta_{face,n})}{90}$$

The Ansys Fluent program uses an alternative approach for the calculation of face non-orthogonality value which aims at capturing additional futures of neighboring cells.

$$\theta_{face} = \left[cos^{-1}\left(\frac{d_{AB} \cdot n}{|d_{AB}||n|}\right), cos^{-1}\left(\frac{d_{AC} \cdot n}{|d_{AC}||n|}\right) \right]$$

This additional term is added because in some cases 2 neighboring cells have n and d_{AB} vectors aligned, nonetheless, the shared face is at a sharp angle. This detail can't be captured by the original definition of face non-orthogonality.

The main problem related to non-orthogonality comes from the fact that its presence increases the strength of the source term, which in turn causes an increase in instability. Below in the table, we have value ranges with acceptance of orthogonality quality.

Excellent	Very good	Good	Acceptable	Bad	Unacceptable
1-0.95	0.95-0.7	0.7-0.2	0.2-0.15	0.14-0.001	0.001-0

Table 3.2 Orthogonality quality values

3.4.2 Mesh with fine element size

The general element size was defined to be 2.5e-003m which meets our needs in terms of meshing quality. Besides, for better capture of angular futures such as rounded surfaces which are existing in the outlet part of the model, Curvature Normal angle was set to 10 degrees.

However, the application of the inflation layer which is directly related to the no-slip condition of fluids on surfaces, due to complexity wasn't possible to be applied and to accommodate for the physical phenomenon and comply with mesh quality, mesh size on regions closer to solid surfaces and problematic parts was reduces to 1.25e-003m through future of Defeature sizing.

Another future that defines mesh quality and transition between cells are Gradient. Its default values are defined to be 1.3, however, experiments with values show that we can adjust it between 1.1-1.3 for better outcomes. In this case, as the size between the minimum and maximum elements wasn't considerably big, its value was set to 1.2. As a result, the total number of nodes is calculated to be 9287161.

Below in photos, we have the zoomed sectional views of the generated mesh, especially the rare part, outlet, and inlet sections. From the shown photos the gradient and defeaturing effects can be clearly recognized.

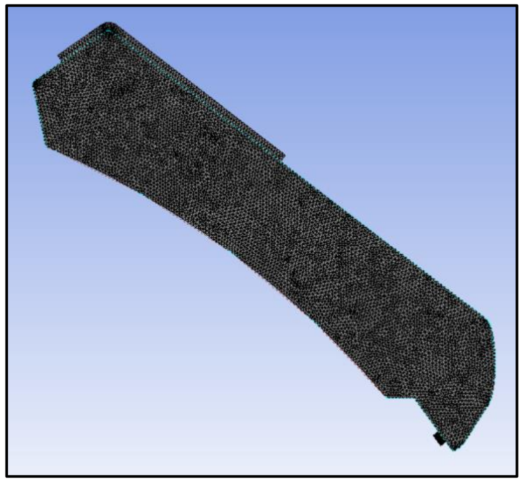

Rare side

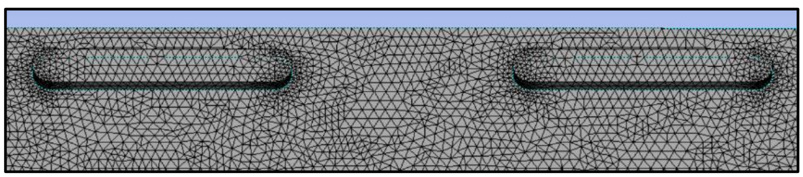

Outlet section

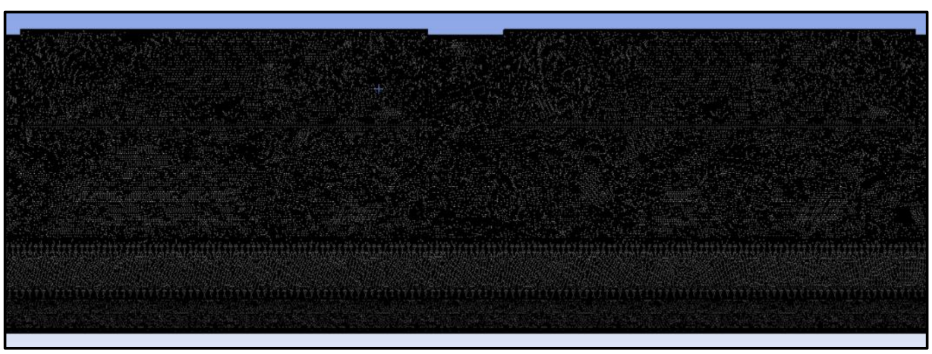

Inlet section

Figure 3.9 Mesh with fine element size

3.4.2.1 Aspect ratio for fine mesh

Below we demonstrate the values of aspect ratio for the fine mesh size. As can be seen, the maximum aspect ratio in our case is around 11.01 which is still in the acceptable region of values. There are only 104 cells possessing indicated high value.

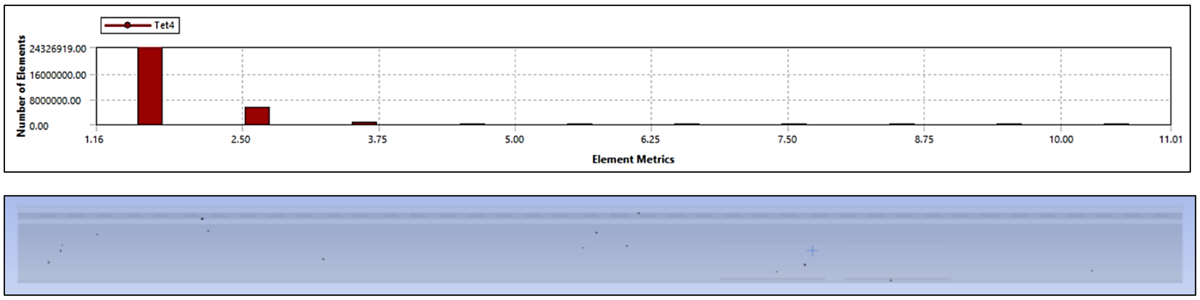

Table 3.3 Aspect ratio for the mesh with fine element size

3.4.2.2 Skewness quality for fine mesh

As it can be seen from the graph, Skewness quality is also in the good region of values. The number of cells with the lowest value of skewness is 4950.

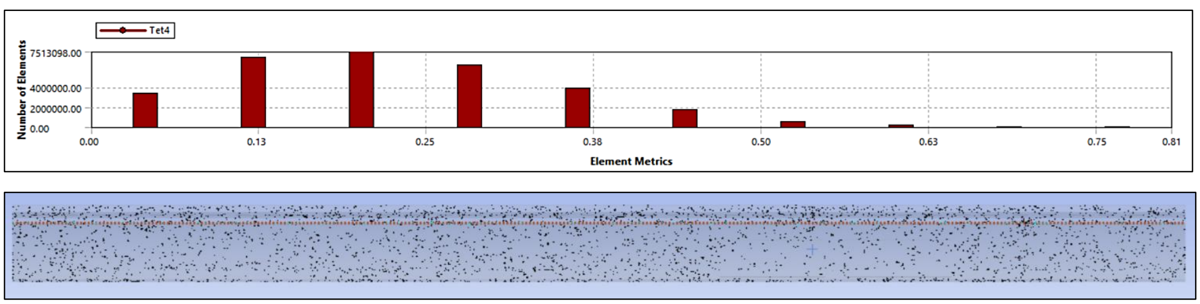

Table 3.4 Skewness quality for the mesh with fine element size

3.4.2.3 Orthogonality quality for fine mesh

The orthogonal quality of the fine mesh also falls into the group of “Good” quality. The number of cells with the lowest orthogonal quality is 4910.

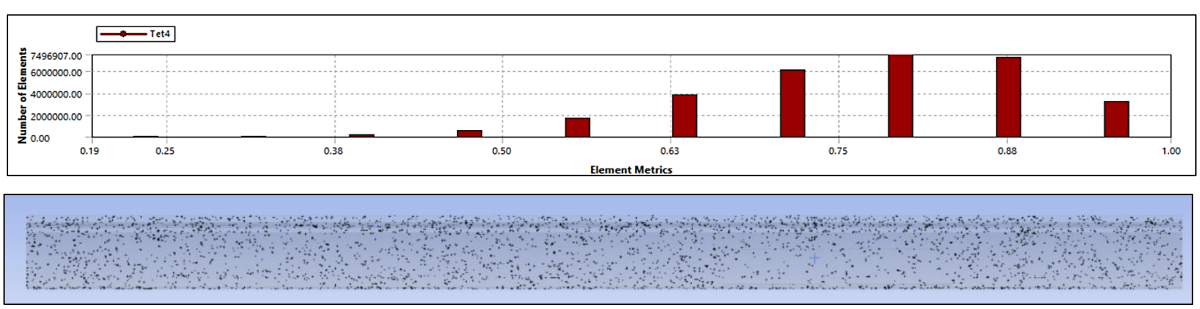

Table 3.5 Orthogonality quality for the mesh with fine element size

Along with the mentioned quality improvement measures, also, to further increase element quality, Smoothing was set to be a high option. Smoothing attempts to improve element quality by moving locations of nodes with respect to surrounding nodes and elements.

Another adjustment that played its role in the adjustment of skewness value is Target Skewness which default value, that is, 0.9 wasn't satisfying for our case at hand, therefore, it was set to a lower limit, that is, to 0.7 to further improve skewness quality.

3.4.3 Medium mesh

For the medium mesh, the size of the element was set to be 7e-003m. As a result, a total number of elements for this new case is 7610060.

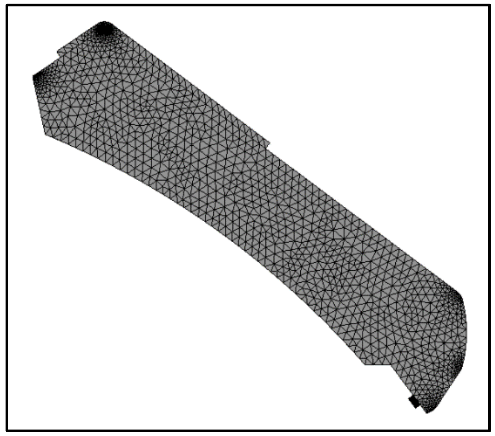

Rare section

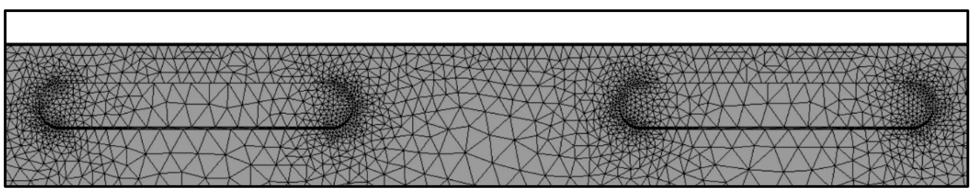

Outlet section

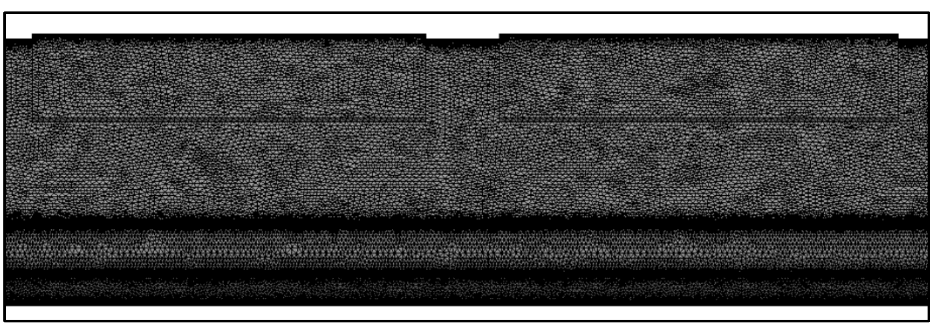

Inlet section

Figure 3.10 Mesh with medium element size

3.4.3.1 Aspect ratio for medium mesh

As it can be seen from the graph the aspect ratio quality is a reasonable range value. The number of elements with the lowest aspect ratio is 5.

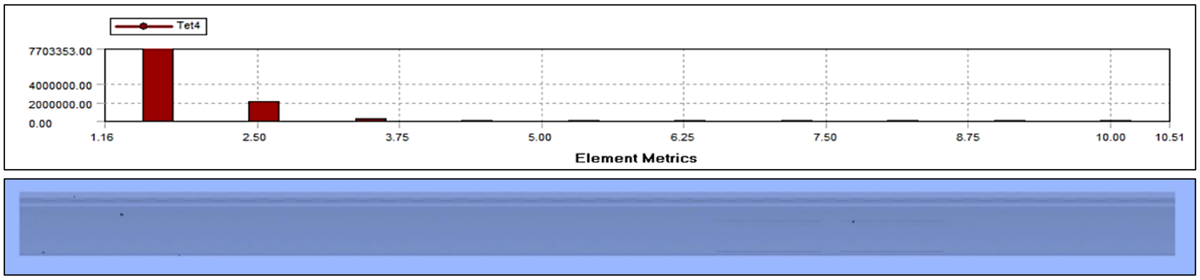

Table 3.6 Aspect ratio for the mesh with medium element size

3.4.3.2 Skewness quality for medium mesh

Skewness quality meets the interest range or values. 3090 elements possess the show lowest quality value.

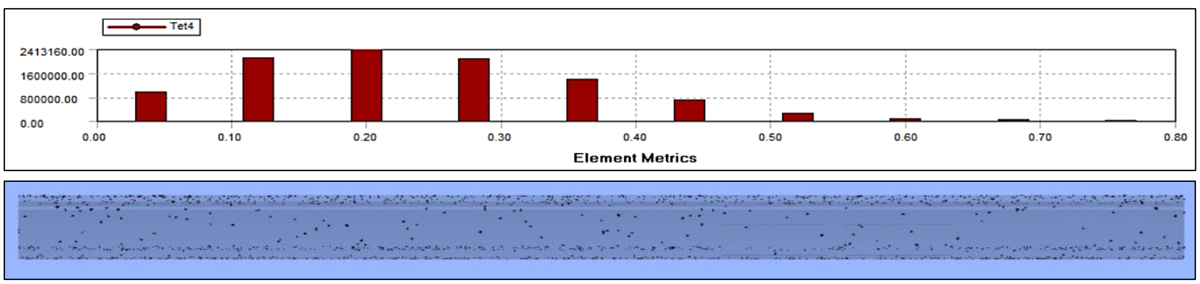

Table 3.7 Skewness quality for the mesh with medium element size

3.4.3.3 Orthogonality quality for medium mesh

Orthogonality quality meets the interest range or values. 3060 elements possess the show lowest quality value.

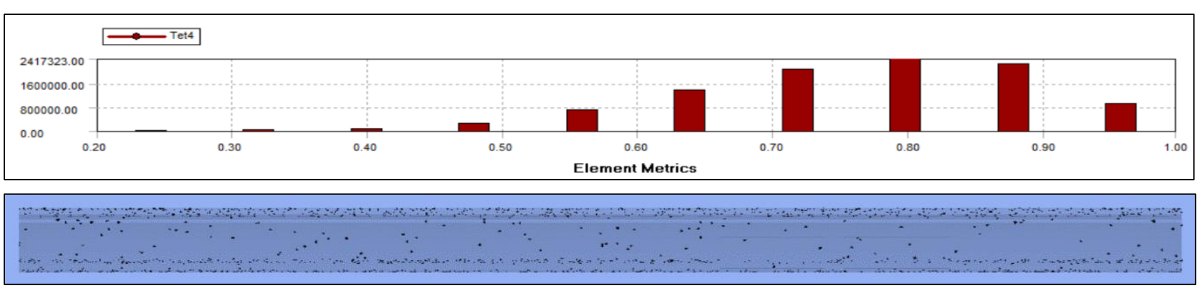

Table 3.8 Orthogonality quality for the mesh with medium element size

3.4.4 Medium mesh 2

For medium mesh 2, the size of the element was set to 1e-002m. As a result, the total number of elements for this new case is 6059131.

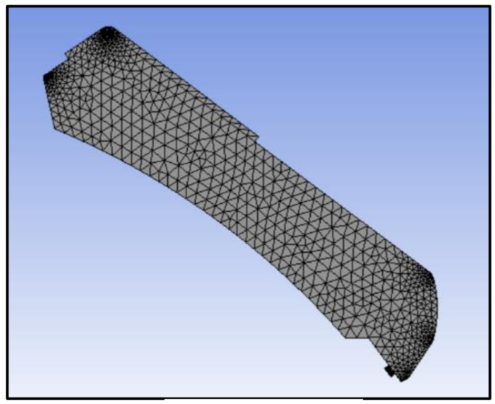

Rare section

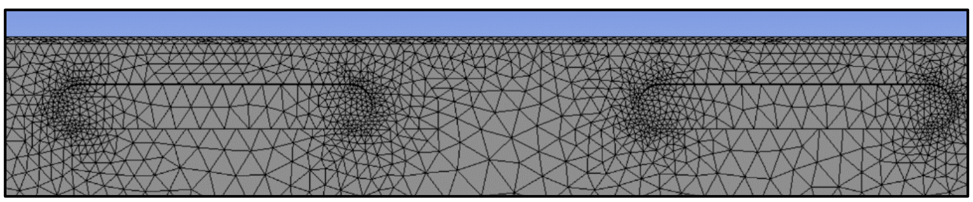

Outlet section

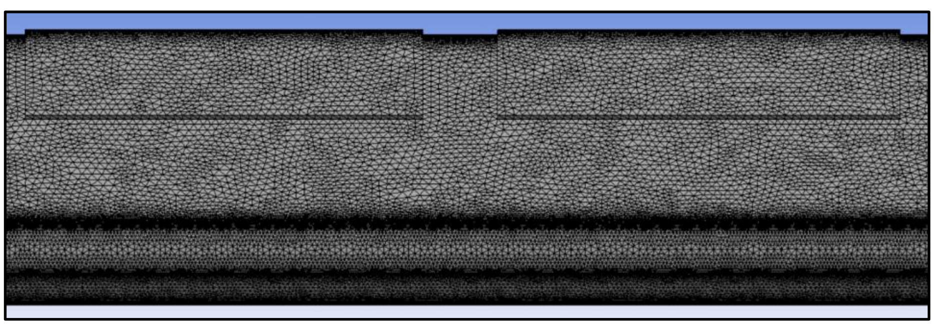

Inlet section

Figure 3.11 Mesh with medium element size

3.4.4.1 Aspect ratio for medium mesh 2

For the medium mesh aspect ratio value also falls within the good region of value, besides the number of elements with the highest aspect ratio being only 4.

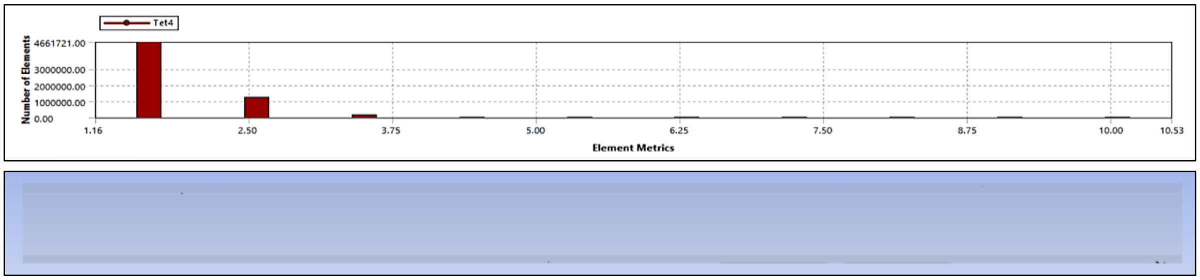

Table 3.9 Aspect ratio for the mesh with medium element size 2

3.4.4.2 Skewness quality for medium mesh 2

Below we see the result for skewness quality. As we can see the skewness value has slightly increased, however, elements with the highest skewness quality still account for a minority of cells, 1120.

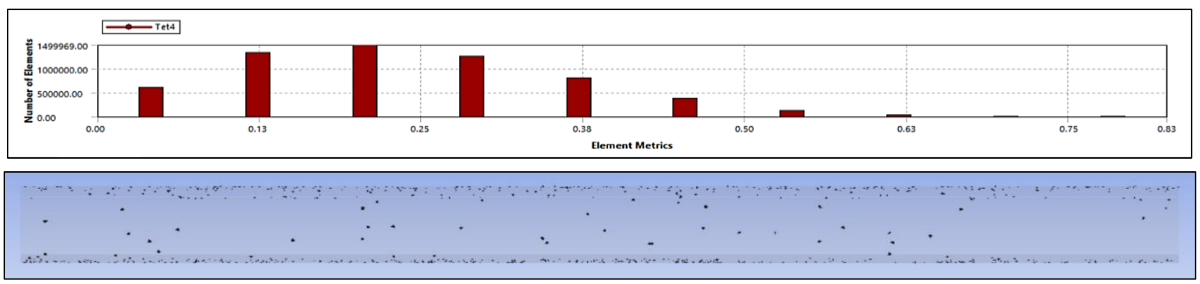

Table 3.10 Skewness quality for the mesh with medium element size 2

3.4.4.3 Orthogonality for medium mesh 2

In the case of orthogonality quality, we see a decrease in quality. For the finest mesh, the minimum orthogonality quality value was limited to 0.19, whereas, in this case, the value decreased up to 0.17. The number of elements possessing the lowest orthogonality quality is 1110.

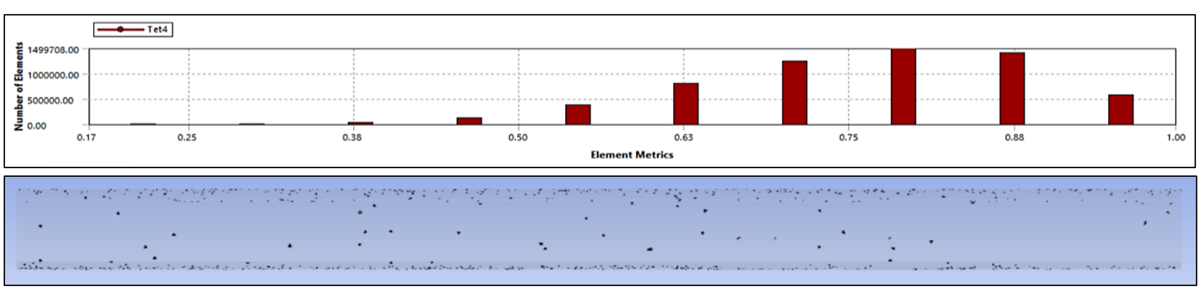

Table 3.11 Orthogonality quality for the mesh with medium element size 2

3.4.5 Coarse mesh

For the coarse mesh, the size of the element was set to be 1.5e-002m. As a result, a total number of elements for this new case is 3077538.

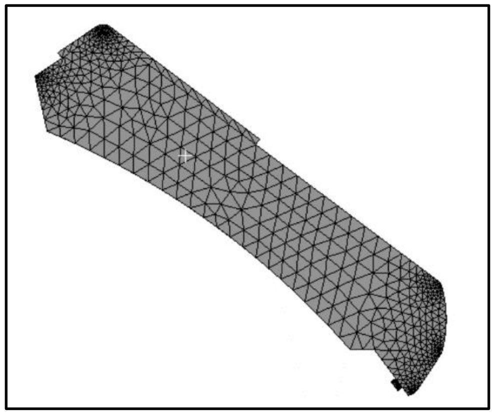

Rare section

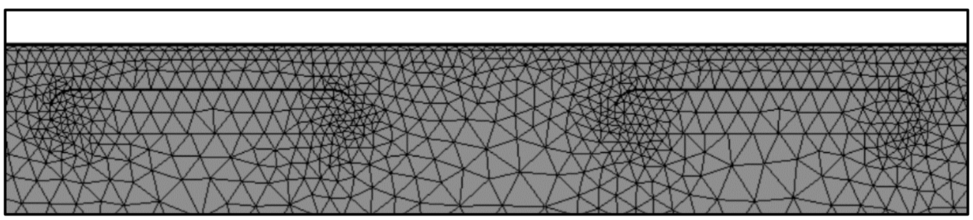

Outlet section

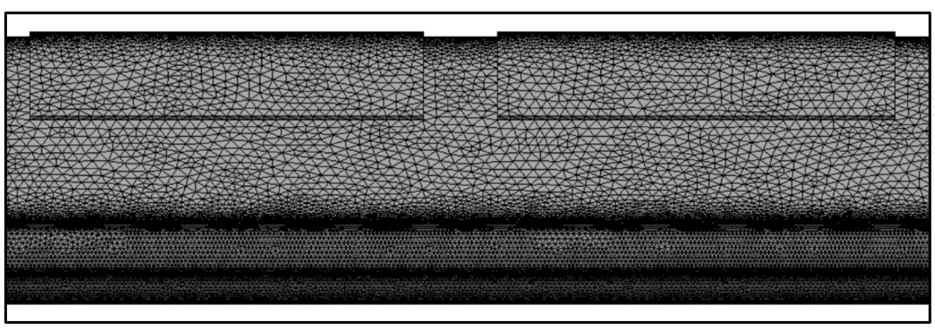

Inlet section

Figure 3.12 Mesh with coarse element size

3.4.5.1 Aspect ratio for coarse mesh

The coarse mesh aspect ratio value also falls within a good region of value, the number of elements with the highest aspect ratio are only 8.

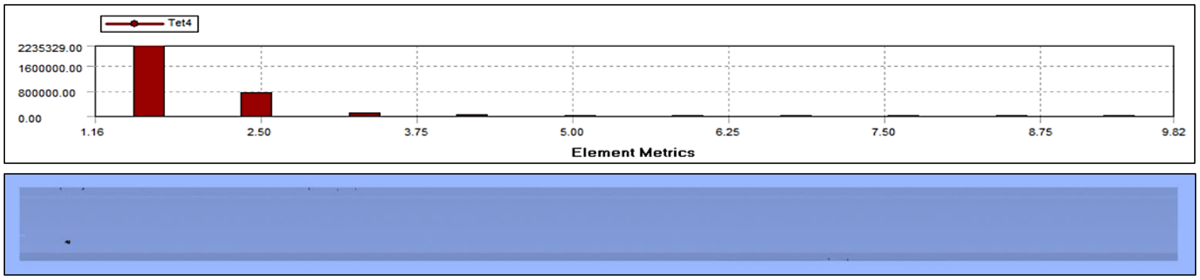

Table 3.12 Aspect ratio for the mesh with coarse element size

3.4.5.2 Skewness quality for coarse mesh

For the coarse mesh, the skewness quality also falls within a good region of the value. The number of elements with the lowest quality is 914.

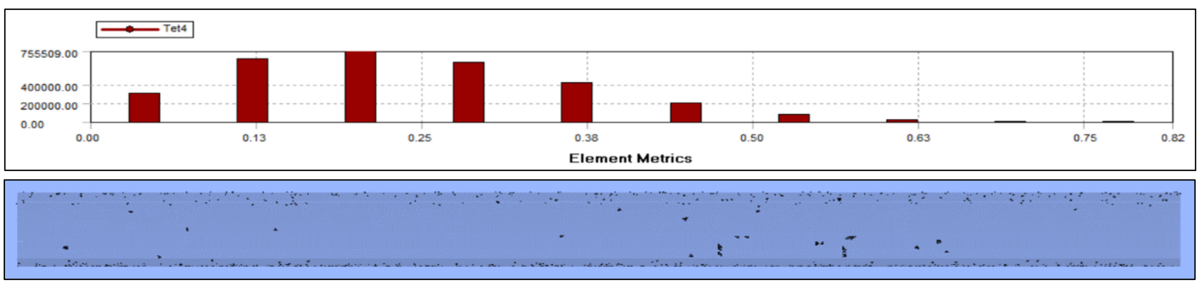

Table 3.13 Skewness quality for the mesh with coarse element size

3.4.5.3 Orthogonality for coarse mesh

The Orthogonality quality also falls within a good region of the value. The number of elements with the lowest quality are 902.

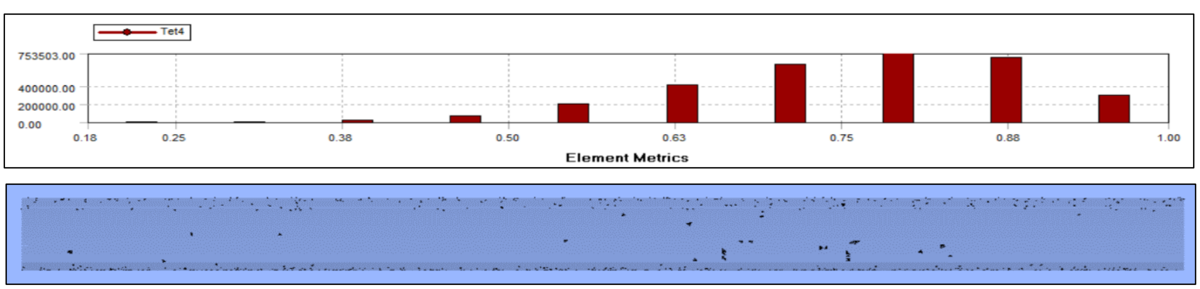

Table 3.14 Orthogonality quality for the mesh with coarse element size

3.4.6 Coarse mesh 2

For coarse mesh 2, the size of the element was set to be 2.5e-002m. As a result, a total number of elements for this new case is 1482045.

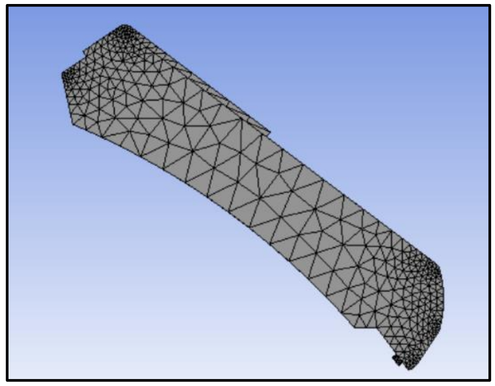

Rare section

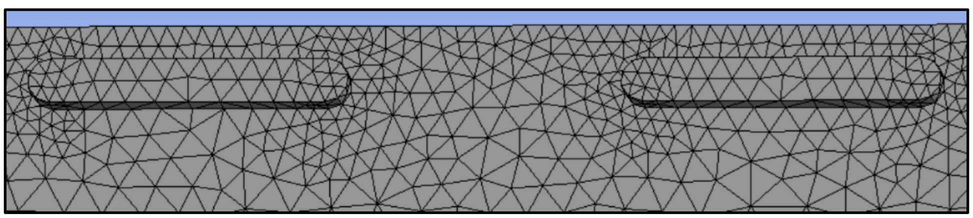

Outlet section

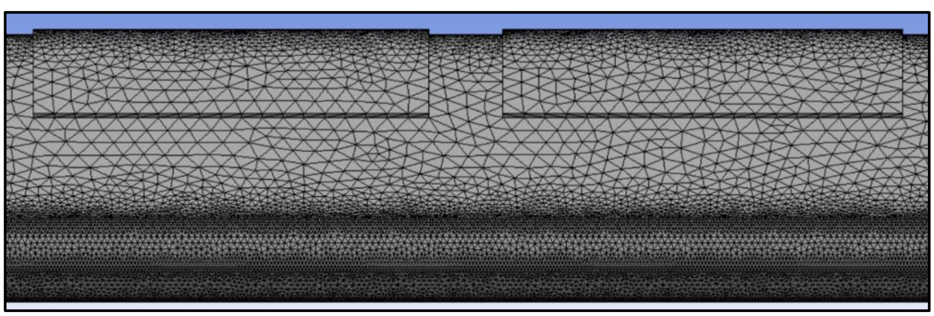

Inlet section

Figure 3.13 Mesh with coarse element size 2

3.4.6.1 Aspect ratio for coarse mesh 2

The coarse mesh aspect ratio value also falls within the good region of value, and even the maximum value decreased compared to the medium case. Besides, the number of elements with the highest aspect ratio is only 6.

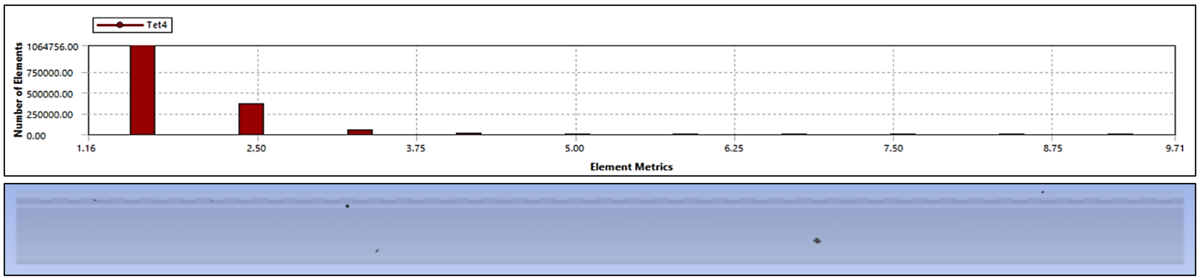

Table 3.15 Aspect ratio for the mesh with coarse element size 2

3.4.6.2 Skewness quality for coarse mesh 2

As we can see the skewness value has slightly decreased also, elements with the highest skewness quality still account for a minority of cells, 318.

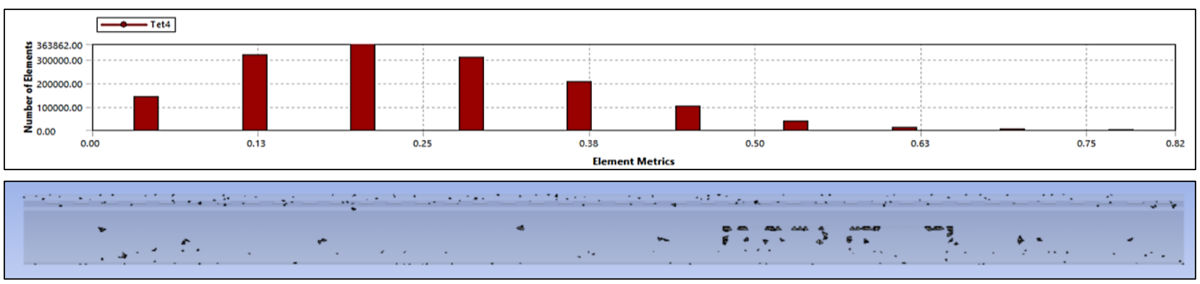

Table 3.16 Skewness quality for the mesh with coarse element size 2

3.4.6.3 Orthogonality for coarse mesh 2

In the case of orthogonality quality, we see a decrease in quality. For the finest mesh, the minimum orthogonality quality value was limited to 0.19, whereas, in this case, the value decreased up to 0.18. The number of elements possessing the lowest orthogonality quality is 311.

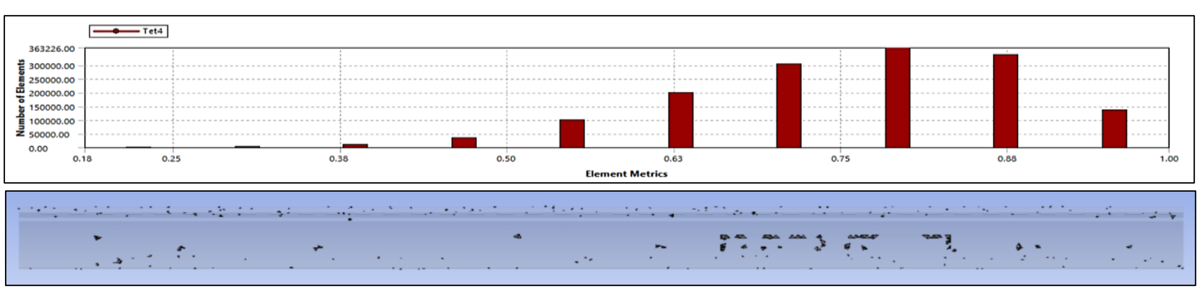

Table 3.17 Orthogonality quality for the mesh with coarse element size 2

3.5 Turbulent flow

There are several Turbulence Models.

Inviscid: is used for the case when the whole domain is accepted to have frictionless flow, potential flow.

Laminar: sets the whole domain to laminar only.

k-ε: is one of the most used models in CFD analysis. This model uses 2 new equations with 2 new unknowns, k, and ε. k-is the turbulence kinetic energy and ε is the dissipated energy. It has three sub-models:1) Standard: not used

2) RNG: suitable for low Re values and more accurate than Standard

3) Realizable: due to its high accuracy is the most used version.

k-ω: is another turbulence model. While k preserves the same meaning, ω is different from ε and it is called dissipated rate. It also has three sub-models:

1) Standard: not used

2) BSL: accuracy-wise has dominance over Standard

3) SST: mostly used version due to highest accuracy.

k-∈ is best suited for flow away from the wall, for example, free surface flow region, whereas the k-ω model is best suited for near the wall flow region, where an adverse pressure gradient is developed. For our investigation, both methods will be used, and a comparison of results will be done.

3.6 Setup of the problem

In the physics of the problem the type of solver brings us two options: 1) Pressure-Based and 2) Density-Based. The difference between these 2 methods is that in the Pressure-Based type we solve continuity and momentum equations simultaneously and in the following step energy and turbulence equations are solved likewise. In the Density-Based type, the equations that are being solved simultaneously are continuity, momentum, and energy equations and they are being followed by the solution of turbulence equations. Initially Pressure-Based was basically designed for low-speed (incompressible) flow, while Density-Based is more appropriate for high-speed (compressible) flow. However, currently, both methods are available for both usages. Nonetheless, the density-based type takes a longer time for the solution of incompressible flow.

In the case under study, for the comfort of users according to experiments, the outlet speed of air from the air channel must be between 2-5m/s. Knowing that to accept compressible fluids as incompressible and make study cases easier, any speed lower than Mach number smaller than 0.3 is accepted to be incompressible. At sea level speed of propagation of sound waves in air is equal to 346 m/s. Going from this point it can be said that the limit value of speed below which air can be considered incompressible is 103.8 m/s. Relying on the theory, in our study we will accept air as an incompressible gas. Therefore, for our purposes, the best solution type is Pressure-Based (Ansys manual).

3.6.1 Velocity formulation

Another aspect of interest is the Velocity formulation type. This module also comes with two options, absolute and relative velocity. Absolute velocities are the ones defined on momentum equations; however, they can be replaced with relative ones as the absolute velocity is considered to be a summation of relative and reference velocities. Despite the fact that relative velocity accelerates the process of convergence, in some cases, it brings about undesired results. Especially, if the velocity change occurs in a small region of the whole domain, error generation is possible. However, a relative type is chosen (Ansys manual).

3.6.2 Material type

In the selection of material type, incompressible air is used. At 15°C air density is 1.255 kg/m3 and dynamic viscosity is 1.81x10-5 kg/m·s. Also, the material which makes up around 90% of the body is made ABS plastic which is also added to the Fluent library for the case under investigation.

3.6.3 Boundary conditions

Inlet boundary condition is defined by the speed of air entering our system. The air conditioning system sends 440m3/h of air to both channels, which means a single channel receives 220m3/h. Air density at 16°C is 1.225 kg/m3. Thus, the mass flow rate which is entering our system is 0.0748611 kg/s. As there are no moving parts inside our domain, the reference frame is set to be the absolute one. Also, the direction of fluid is set to be normal to the boundary. As our case is considered to be a free stream, we set turbulence intensity at %5 and turbulence viscosity ratio to 10.

The most suitable boundary for outlet boundary conditions, in this case, is the pressure-outlet type. At this point, we set Gauge pressure to 0, which means we make absolute pressure equal to atmospheric pressure at the outlet section. Also, the flow direction on the outlet section is set to be normal to the boundary face. Backflow Pressure specification is set to Total pressure to make the backflow possess the properties of velocity and pressure of the outlet section. In wall boundary condition the two important things that have to be defined are No-slip condition and Stationary wall status.

3.6.4 Solution method

Solution methods also have several options which varies depending on application type:

1) SIMPLE: is suitable for low Re values, and simple geometry problems.

2) SIMPLEC: is more suited for complicated flow types compared to simple. Also, good for high Re values. However, this model might lead to instability if mesh quality is not sufficient.

3) PISO: usually recommended for Transient problems with large time steps.

4) Coupled: usually recommended for Transient problems with small time steps.

SIMPLE, SIMPLEC, and PISO are called segregated schemes and they calculate pressure from continuity equation followed by velocity calculated from momentum equations. However, Coupled scheme do both calculations simultaneously and yields more accurate results. For our project, we use SIMPLEC as an optimal option.

Another selection suggested by the manual is to use Green-Gauss Node Based gradient type for non-structured grids.

3.6.5 Residual’s value

Residuals in the solver are the main source of checking the convergence of solutions. They are defining the errors at each node at each iteration. However, in the convergence process, the residuals graphs don’t give the error at each cell. Rather, CFD programs use a different approach in which first Representative residuals which can be defined through methods, such as L_1, L_2, and L_∞, are defined, and then Scaled residuals values are plotted on the convergence graphs. Representative residuals represent the residuals in all the cells in the mesh.

One of the simplest methods of definition of residual values is the L2 method in which all residual values are calculated, and then their square is summed under the square root. After this, the generated value is divided by the square root of several cells.

However, the Representative residual is not the value monitored in convergence graphs. It is the Scaled residual value. For a heat conservation equation, it can be defined as the ratio between the residual (lack of energy disappearing unreasonably) and flux of heat going through a cell. Most of the CFD programs handle the indicated process automatically.

Mass in balance or Continuity residuals are treated differently from the other residuals. For their determination Normalization process is used. Every single new value of residual is divided by the maximum value on the graph and this process is called Normalization. As we solve that CFD solution, mass imbalance reduces.

Another aspect is with the iterative approach it is not possible to reach zero value for residuals.

Several residuals are being defined by the user and there can be 2 distinct cases in the convergence process:

1) The number of residuals keeps decreasing up to a particular value and then becomes stable, and no further fluctuation is seen on our curves.

2) The number of residuals keeps decreasing; however, the user sets a particular limit value, and the values below the shown threshold are not in the user's area of interest.

In our case, as the program manual suggests, we will set a residual's RMS value and examine the trending of curves on Convergence History. In our case, the number of residuals is set to be 0.0001 for all unknowns.

3.6.6 Initialization

In initialization, we have 2 types: Hybrid and Standard. However, there is no specific rule defining their usage cases. As Hybrid is an automatic method of initialization, for the purpose of simplicity, we use it in our project.

3.7 Mesh Independency analysis

Below we illustrate the plots of convergence of residuals, the average volume pressure change, and mass flow rate at the outlet of the air channel. These analyses have been done for all five mesh structures to prove the mesh independency from the results.

3.7.1 Fine mesh

In the case of fine mesh, all the residuals have reached the convergence conditions which were set to 10-4. Besides, as it can be seen from the graph, pressure, and mass flow rate values have also stabilized and the mass flow rate at the outlet section reached the value of 7.4861e-02 kg/s which is the same as the inlet mass flow rate condition. Besides average and maximum speeds of fluid at the outlet section for fine mesh are defined to be 2.75217m/s and 4.313m/s correspondingly.

Continuity	X velocity	Y velocity	Z velocity	k	ϵ
6.0677e-05	2.7377e-08	2.5935e-08	2.5318e-08	1.2187e-05	2.3705e-05

Table 3.18 Residual values for fine mesh study

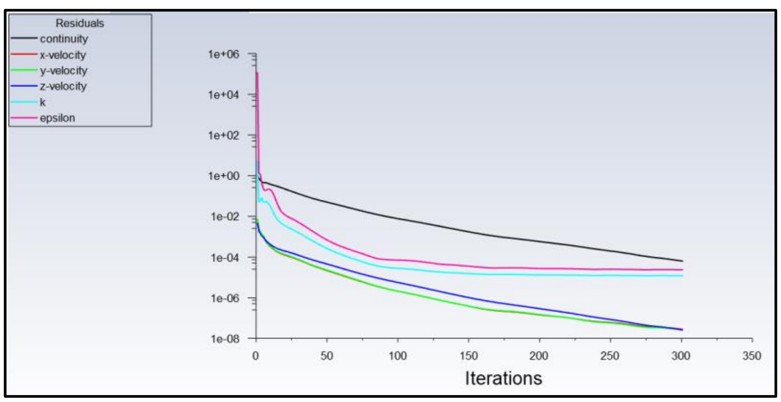

Figure 3.14 Residuals graph of fine mesh study

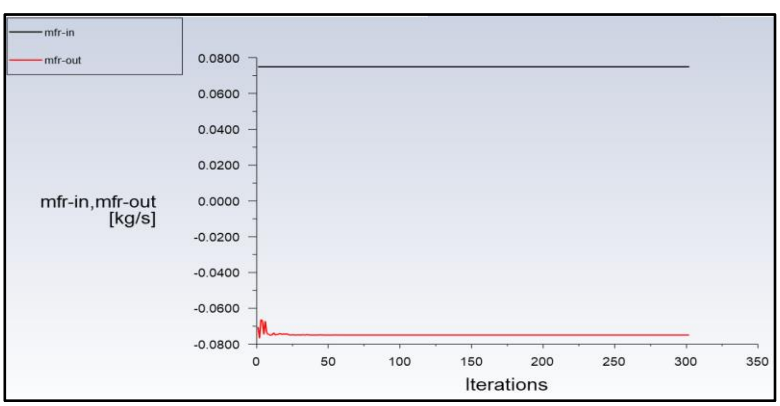

Figure 3.15 Mass flow rate graph of fine mesh study

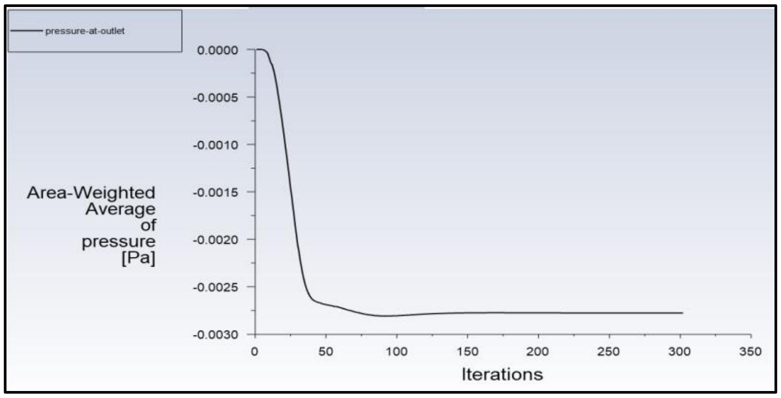

Figure 3.16 Average pressure graph of fine mesh study

3.7.2 Medium mesh

For medium mesh, all the residuals have reached the convergence conditions which were set to 10^{-4}. Besides, as it can be seen from the graph, pressure, and mass flow rate values have also stabilized and the mass flow rate at the outlet section reached the value of 7.4861e-02 kg/s which is the same as the inlet mass flow rate condition. Besides average and maximum speeds of fluid at the outlet section for fine mesh are defined to be 2.75109m/s and 4.317m/s correspondingly.

Continuity	X velocity	Y velocity	Z velocity	k	ϵ
7.0973e-05	3.9977e-08	3.6831e-08	3.6319e-08	1.4189e-05	2.7904e-05

Table 3.19 Residual values for medium mesh study

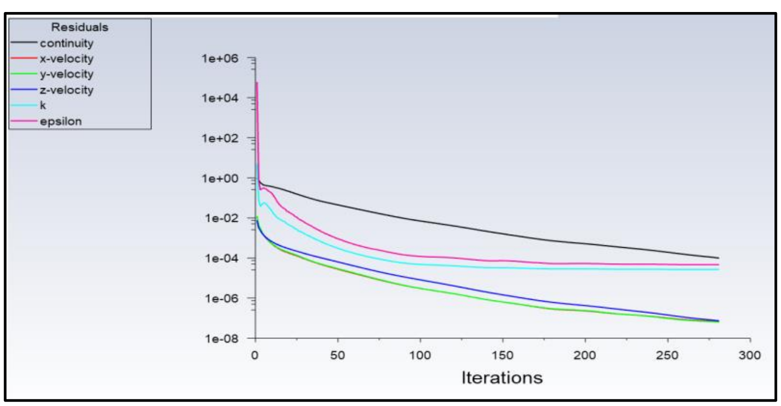

Figure 3.17 Residuals graph of medium mesh study

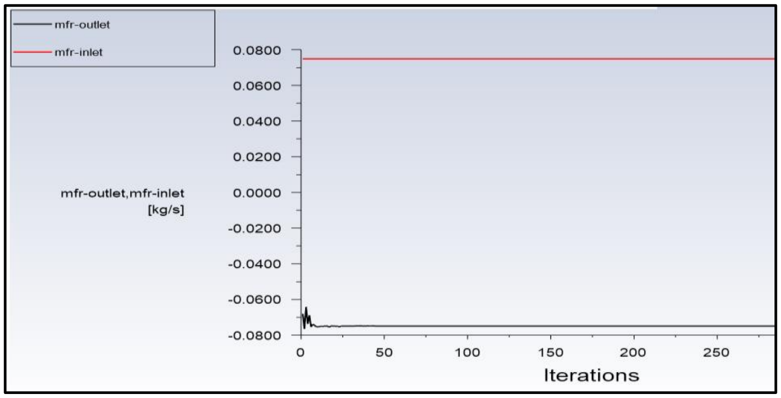

Figure 3.18 Mass flow rate graph of medium mesh study

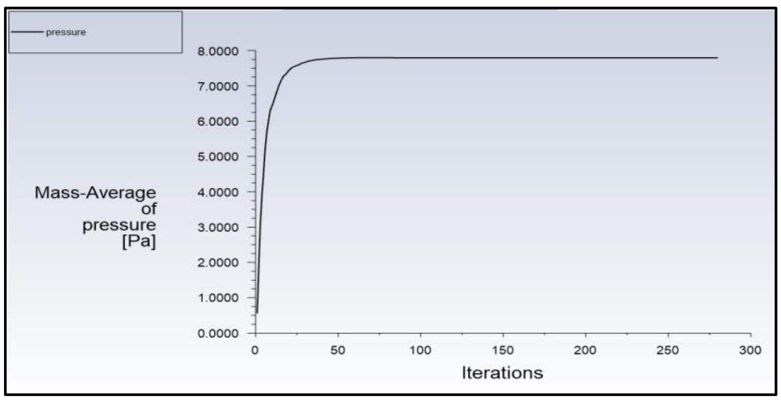

Figure 3.19 Average pressure graph of medium mesh study

3.7.3 Medium mesh 2

As far as medium mesh 2 is regarded all the residuals have reached the convergence conditions which were set to 10^{-4}. Besides, as it can be seen from the graph, pressure, and mass flow rate values have also stabilized and the mass flow rate at the outlet section reached the value of 7.4861e-02 kg/s which is the same as the inlet mass flow rate condition. Besides average and maximum speeds of fluid at the outlet section for fine mesh are defined to be 2.75088/s and 4.331m/s correspondingly.

Continuity	X velocity	Y velocity	Z velocity	k	ϵ
8.0163e-05	3.8241e-08	3.6211e-08	3.5428e-08	1.4189e-05	2.7904e-05

Table 3.20 Residual values for medium mesh study 2

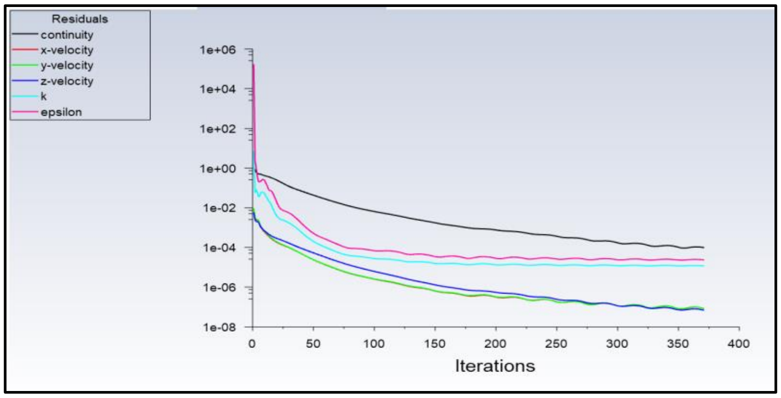

Figure 3.20 Residuals graph of medium mesh study 2

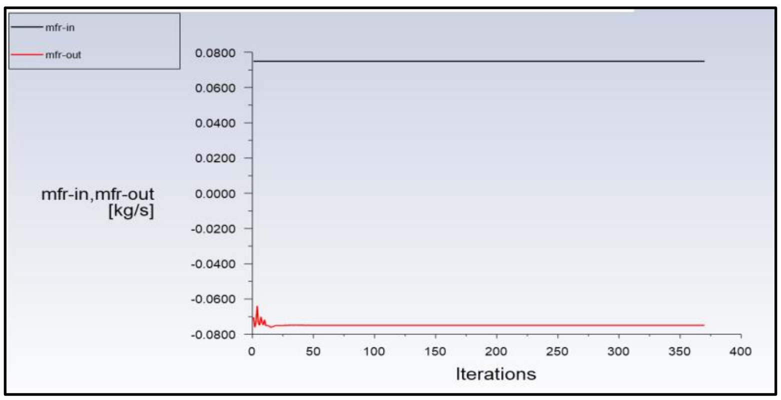

Figure 3.21 Mass flow rate graph of medium mesh study 2

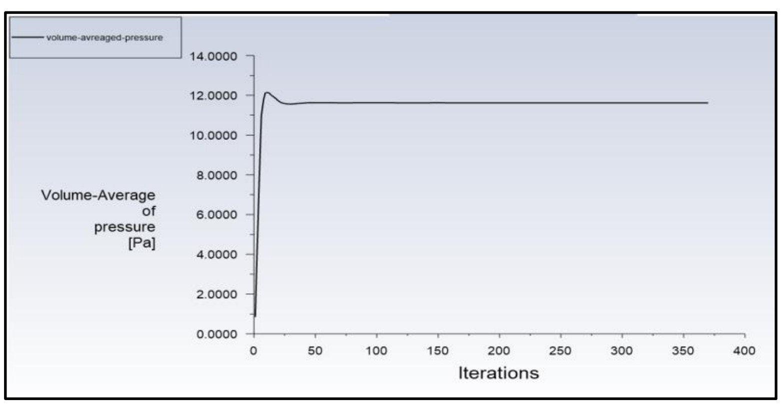

Figure 3.22 Average pressure graph of medium mesh study 2

3.7.4 Coarse mesh

The coarse mesh also meets the residuals' convergence condition which was set to 10^{-4}. Also, as it can be seen from the graph, pressure, and mass flow rate values have also stabilized and the mass flow rate at the outlet section reached the value of 7.4861e-02 kg/s which is the same with the inlet mass flow rate condition. Furthermore, average and maximum speeds of fluid at the outlet section for fine mesh are defined to be 3.01929m/s and 4.204m/s correspondingly.

Continuity	X velocity	Y velocity	Z velocity	k	ϵ
8.1397e-05	5.1666e-08	5.4598e-08	7.4947e-08	1.3556e-05	2.2563e-05

Table 3.21 Residual values for coarse mesh study

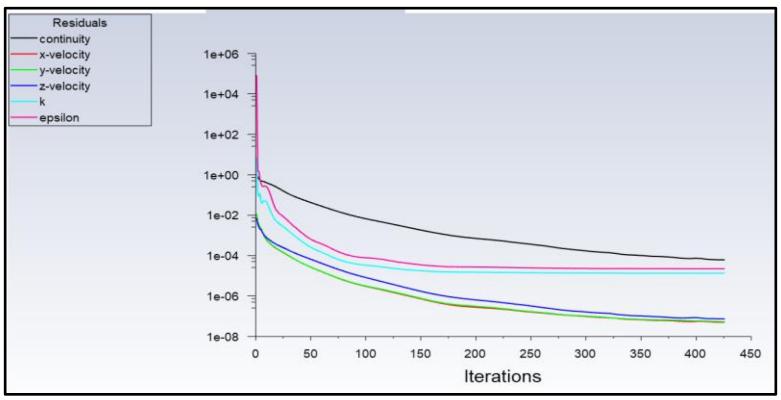

Figure 3.23 Residuals graph of coarse mesh study

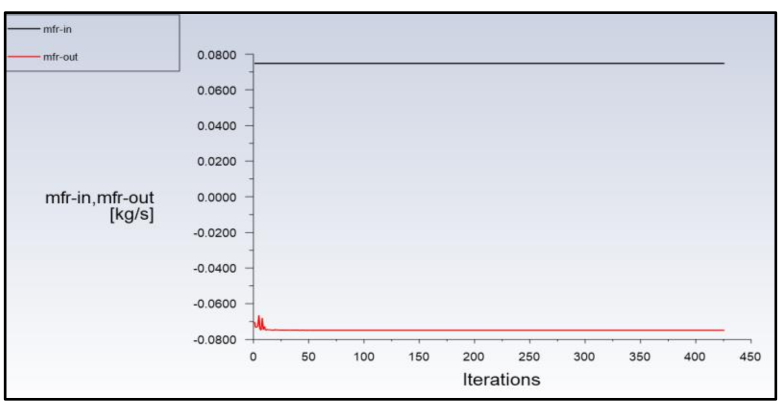

Figure 3.24 Mass flow rate graph of coarse mesh study

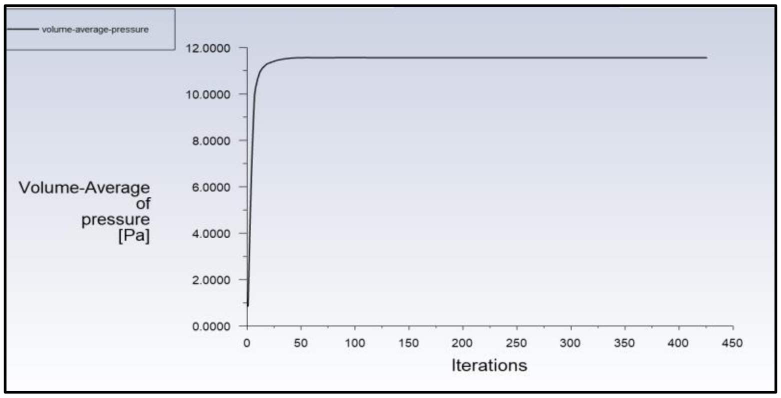

Figure 3.25 Average pressure graph of coarse mesh study

3.7.5 Coarse mesh 2

Coarse mesh 2 also meets the residuals' convergence condition which was set to 10^{-4}. Also, as it can be seen from the graph, pressure, and mass flow rate values have also stabilized and the mass flow rate at the outlet section reached the value of 7.4861e-02 kg/s which is the same as the inlet mass flow rate condition. Besides average and maximum speeds of fluid at the outlet section for fine mesh are defined to be 3.18918m/s and 4.202m/s correspondingly.

Continuity	X velocity	Y velocity	Z velocity	k	ϵ
8.0211e-05	3.9221e-08	3.7233e-08	3.6429e-08	1.4189e-05	2.7904e-05

Table 3.22 Residual values for coarse mesh study 2

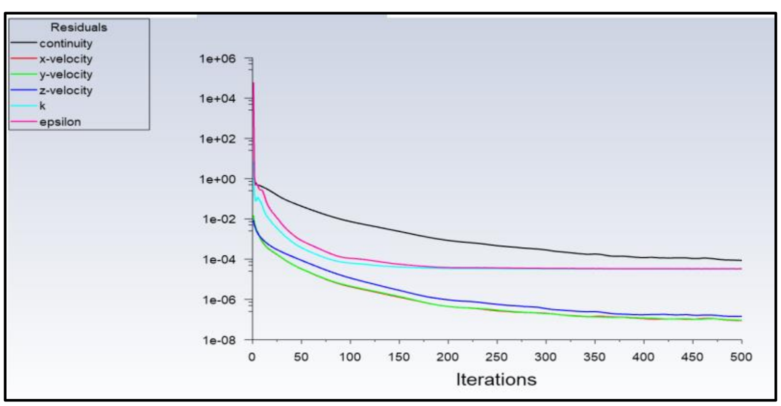

Figure 3.26 Residuals graph of coarse mesh study 2

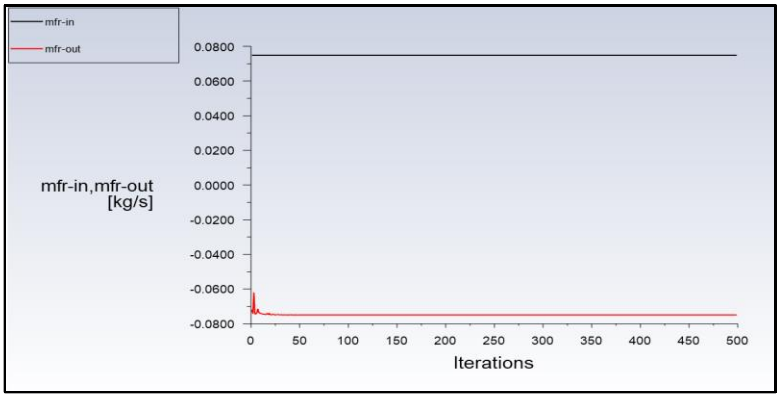

Figure 3.27 Mass flow rate graph of coarse mesh study 2

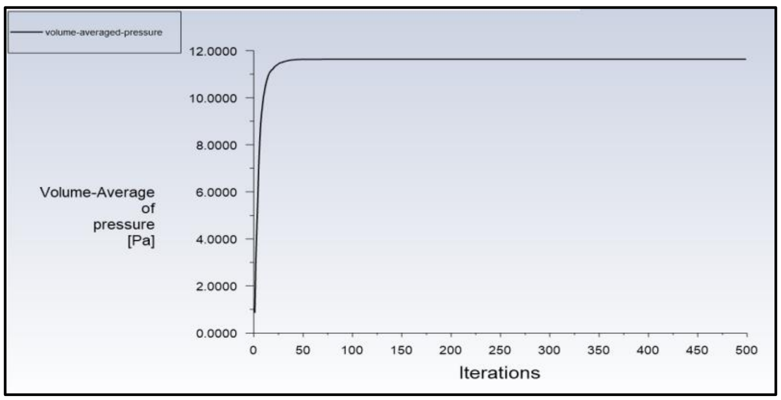

Figure 3.28 Average pressure graph of coarse mesh study 2

3.7.6 Mesh Independency

According to the outcomes of the 5 mesh analysis, for each mesh, the average output speed at the outlet is shown in the table below.

Fine mesh	Medium mesh	Medium mesh 2	Coarse mesh	Coarse mesh 2
2.75217m/s	2.75109m/s	2.75088/s	3.01929m/s	3.18918m/s

Table 3.23 Average outlet speed for meshes

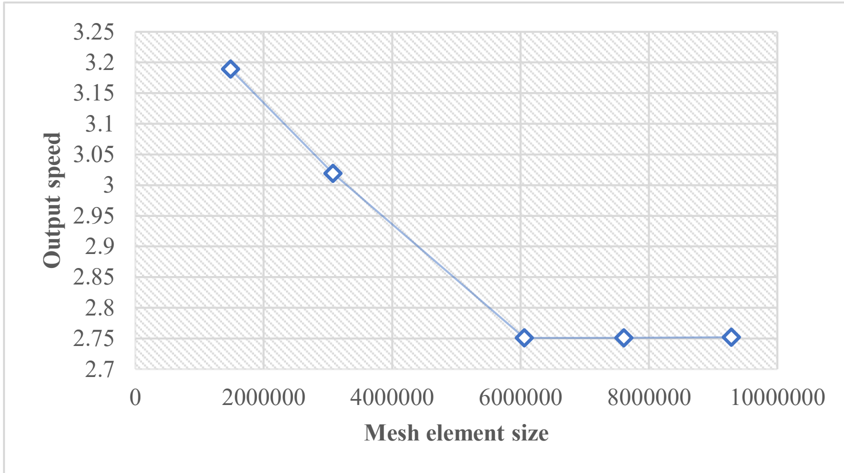

Figure 3.29 Output speed vs mesh element size

Examining the shown graph, it can be concluded that after 6 million nodes the change in output value dramatically decreased. However, below 6 million nodes, which is corresponding to the size of medium mesh 2, there is a difference between outcomes. Nevertheless, the percentage of variation of the outcome between fine and coarse meshes is only 8.84%. In the case of comparison between fine and medium mesh, this value drops down to 0.03%. Thus, it can be concluded that the mesh is solution independent and for further analysis, fine mesh size is used.

3.7 Verification and Validation

Before the acceptance of the results of a CFD study, Verification and Validation processes must be conducted. These two processes have different purposes of application. Verification is a process regarding the setup process of a problem, that is, whether the correct boundary conditions, equations, and parameters are used. Meanwhile, Validation is a process of assessment of the accuracy of a process and its comparison with experimental results. Commercial CFD programs, such as Ansys, verification process of equations is conducted by the code vendor. However, still, the author should make verify of other mentioned processes.

In the verification process we are making a comparison between CFD and experimental results and apply different turbulence models and other parameters to see which model brings about the closest representation of reality. Demonstrating the level of accuracy in CFD analysis is a complicated process as there are many sources of error. Below we have the lift of some error types:

1. Physical approximation error

- Physical modeling error
- Geometry modeling error

2. Computer round-off error
3. Iterative convergence error
4. Discretization error
   - Spatial discretization error
   - Temporal discretization error
5. Computer programming error
6. Usage error

Mentioned errors affect the accuracy of CFD studies. In this study, we will first examine the source of error that occurred because of mesh sizing. The geometrical simplifications are not going to be examined as in this study there wasn't a geometry simplification.

3.7.1 Determination of output speed of mesh with infinite element number

To have an ideal CFD mesh the number of cells must be infinite. However, it is not possible to reach this high value of cells. As it is impossible to reach an infinite number of cells there is an error associated. This error is called the Discretization error. To define the discretization error, we use a mesh refinement study. Once we define the discretization error, a choice of adequate mesh can be done which can be also used for future studies.

Here we have the discretization error expression. It is defined as the difference between a CFD solution and a real solution:

$$\mathrm{d} = \Psi - \Psi_{\mathrm{CFD}}$$

CFD domain is composed of mesh cells. Inside these cells, flow variables vary linearly. However, in reality, properties don't vary linearly over a distance. To accommodate the generated real profile, the Tailor series should be used:

$$\Psi = c_0 + c_1 x + c_2 x^2 + c_3 x^3 + \cdots$$

Here x is the distance from the sampling point and c values are coefficients that are used to fit a polynomial to the real temperature profile at hand. However, for a CFD domain, as properties vary linearly, expression can be written the following way:

$$\Psi_{\text{CFD}} = c_0 + c_1 x$$

From this point, we see that discretization error is proportional to the square of the distance. Therefore, a decrease in the distance by half will cause four times to decrease in the error. In CFD codes linear approximation is made by the distance between cell centroids, m. Hence, decreasing cell size will affect the distance m, and reduce the discretization error. Going on from this point, it is stated that in an ideal CFD solutions are described as second-order accurate, despite the fact that variation across a cell is linear. It brings to the outcome of order stating that the order of accuracy is, b=2. However, this order of accuracy in CFD solutions is reduced and is not equal to 2 as in the case of the Ideal CFD solution. It is associated with the fact that sometimes to eliminate the generation of divergence of solution modification of variables along a cell is implemented. Some methods which significantly affect the linear variation of variables along a cell are noted below:

- Upwind differencing
- Skewness error
- Gradient limiters

Because of upwind differencing, gradient limiters, and other sources of reduced accuracy, real CFD solutions are less than second-order accurate ($b < 2$). As gradient limiters, upwind differencing and other numerical methods affect the order of accuracy, the order of accuracy cannot be determined before the CFD calculations are carried out. The order of accuracy and the discretization error is calculated as part of a mesh refinement study.

To be able to track mesh sensitivity study, first, it is compulsory to define a representative length of a cell in the mesh. Here, rather than using N, a number of elements in our mesh, we use d. It comes from the fact that if we have an infinite number of cells, N will go to infinite, however, d will go to 0. Below the expression of d for 3D bodies is given:

$$d = \left[\frac{1}{N}\sum_{cell} V_p\right]^{1/3}$$

On the formula, Vp is the volume of a cell, and N is the number of cells. In the mesh refinement studies, we must examine at least 3 different meshes that have different levels of refinement. In the paper of Celik et al.(2008) notes that the difference between the representative cell lengths should be at least 30%. To check the difference, we should use the refinement ratio which is the ratio between cell representative lengths.

$$r = \frac{d_{coarse\ mesh}}{d_{medium\ mesh}} > 1.3$$

Below we demonstrate the representative length and refinement ratio values for our cells. The volume of our body is 0.1971m3. For our cells the number o nodes are Nf= 9287161, Nm= 6059131, Nc = 1482045.

$$d_{coarse\ mesh} = 0.005104365;\ d_{medium\ mesh} = 0.003192215\ ;\ d_{fine\ mesh} = 0.002331511$$

$$r_1 = \frac{d_{coarse\ mesh}}{d_{medium\ mesh}} = 1.599\ \ ;\ r_2 = \frac{d_{medium\ mesh}}{d_{fine\ mesh}} = 1.369$$

As both values are higher than the threshold value, 1.3, the indicated mesh sizes can be used for further investigation of the study.

The next step is the determination of the d value of a mesh made of an infinite number of elements. The most popular method which is based on extrapolation is the method proposed by Richardson (1910, 1927). This application is also suggested by the Journal of Fluids Engineering. The relationship between the solution variable and the representative cell length h depends on the quantity being. To fit a function to this data is the fundamental tenet of Richardson extrapolation. The value at h = 0 may then be calculated using the function to extrapolate (the solution on an infinitely fine mesh). A universal polynomial of h would be the simplest function:

$$\Psi = \Psi_0 + c_1 d + c_2 d^2 + c_3 d^3 \dots$$

In an ideal situation, fluctuates proportionally to d^2 and ideal CFD calculations are second-order accurate. Consequently, we could only use a polynomial of second order:

$$\Psi = \Psi_0 + c_2 d^2$$

However, as was covered in the preceding section, second-order precision is not typically achieved by genuine CFD computations. Because of this, the fitting function must permit to fluctuate at a lower rate than d^2. It would thus be preferable to employ a power-law function:

$$\Psi = \Psi_0 + c d^p$$

where c is a constant that is used to fit the function to the data, and p is a positive real value. The ideal situation, where p = 2, as well as actual CFD scenarios, where p is less than 2, may both be solved using the power-law function. The mesh refinement study's order of convergence or order of precision is denoted by the parameter p.

The answer may be extrapolated to an indefinitely fine mesh (Ψ_0) once the power-law function has been fitted to the mesh refinement research. The order of convergence (p), however, had to be determined in order to complete the extrapolation. Utilize the values that were computed on the fine and medium meshes to determine Ψ_0. For the fine mesh we outcome is $\Psi_1 = 2.75217 \mathrm{m/s}$ and for medium mesh Ψ_2 = 2.75088m/s.

$$\Psi_2 = \Psi_0 + cd_1^p \quad and \quad \Psi_3 = \Psi_0 + cd_2^p$$

To eliminate c from the equation, we combine 2 solutions together:

$$c = \frac{\Psi_2 - \Psi_0}{h_1^p} \quad \rightarrow \quad \Psi_0 = \frac{\left(\frac{d_2}{d_1}\right)^p \Psi_2 - \Psi_3}{\left(\frac{d_2}{d_1}\right)^p - 1}$$

Further simplification can be done by application of r_2 which were defined as d_2/d_1:

$$\Psi_0 = \frac{(r_2)^p \;\; \Psi_2 - \Psi_3}{(r_2)^p - 1}$$

Then, to further simplify the case, and modify it for suitable use the numerator was added, and extracted the term Ψ_2:

$$\Psi_0 = \frac{(r_2)^p \;\; \Psi_2 - \Psi_3 - \;\; \Psi_2 + \;\; \Psi_2}{(r_2)^p - 1} \rightarrow \Psi_0 = \;\; \Psi_2 + \frac{\Psi_2 - \Psi_3}{(r_2)^p - 1}$$

However, for the calculation of Ψ_0, we must define p. Celik et al. (2008) propose a more general method to determine the order of convergence which is applicable to both monotonic and oscillatory convergence. For the application of the method, first, we have to define the difference between the solution of fine and medium, medium and coarse.

$$\epsilon_{21} = \Psi_2 - \Psi_1 = -0.4383 \quad and\; \epsilon_{32} = \Psi_3 - \Psi_2 = 0.00129$$

Then we must define a variable $s = sign\left(\frac{\epsilon_{32}}{\epsilon_{21}}\right) = sign(-0.00294319) = -1.$ If the ratio is positive, then the convergence is monotonic since ϵ_{21} and ϵ_{32} have the same sign. If the ratio is negative, the convergence is oscillatory and the signs of ϵ_{21} and ϵ_{32} are opposite. The two linked equations presented by Celik et al. (2008) may be solved to determine the order of convergence regardless of whether the convergence is monotonic or oscillatory:

$$p = \frac{1}{\ln(r_{21})}\left|\ln\left|\frac{\epsilon_{32}}{\epsilon_{21}}\right| + q\right| \quad and \quad q = ln\left(\frac{r_{21}^{p} - s}{r_{32}^{P} - s}\right)$$

However, it is possible to rearrange these two equations together and find a single solution:

$$\frac{1}{\ln(r_{21})}\left|\ln\left|\frac{\epsilon_{32}}{\epsilon_{21}}\right| + ln\left(\frac{r_{21}^{p} - s}{r_{32}^{P} - s}\right)\right| - p = 0$$

This is the general form of a non-linear equation that can be solved with a root-finding algorithm f(p) = 0. Therefore, we have used a proposed excel sheet by Celik, and have defined our value of $p = 1.98$ and $\Psi_0 = 2.7436$ m/s. Below, in Figure 3.28 demonstration of d values with respect to Ψ values can be seen. For the mesh with the infinite number of elements the representative length, d, is zero.

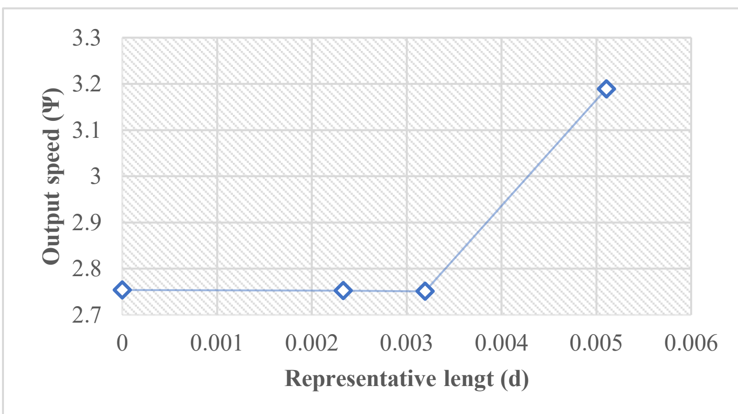

Figure 3.30 The relation between representative length and output speed

3.7.2 Determination of mesh error

As the number of elements in the case of fine mesh is not equal to infinite, the output speed is affected by the number of cells. Therefore, we determine the error of the fine mesh with respect to infinite cell mesh with the help of the following equation:

$$E = |(\Psi_1 - \Psi_0)/\,\Psi_0\,| = 0.3\%$$

This is called the Extrapolated relative error.

3.8 The choice of turbulence model

After finishing the mesh refinement process, the next step is the choice of the right turbulence model which can also affect the outcome. However, this process must be conducted after the mesh refinement processes. If we examine the comparison between experimental results and infinite mesh output, there is no doubt that there is an error between the values. This error can be caused by the turbulence model applied, or simplifications did on geometry.

The ability to calculate different turbulence models for different studies changed. Below we list several application cases for turbulence models:

- Spalart Allmaras model for attached aerodynamic flows
- Reynolds Stress Transport Models for flows which have high swirl and anisotropy
- The $k - k_L - \omega$ and $\gamma - Re_\theta$ for flows with laminar and transitional flow regions
- Large Eddy Simulation (LES) if the calculation is feasible with the available computation resources

However, to understand which model gives the best outcome, the first experiment on different models must be conducted. However, in almost all cases, k-ϵ and k-ω SST models are the best starting points. They succeed in a wide range of scenarios. Therefore, in this study applies a comparison between these 2 models is conducted.

3.8.1 k-∈ model

In the Reynold averaged Navier-Stokes equations, RANS, there is an additional term called Reynolds-stress. This expression is made of the product of two fluctuating velocity components.

$$\frac{\partial(\rho V)}{\partial t} + \nabla \cdot (\rho V V) = -\nabla P + \nabla \cdot [\mu(\nabla V) + (\nabla V)^T] + \rho g - \nabla\left(\frac{2}{3}\mu(\nabla \cdot \mathrm{V})\right) - \nabla \cdot (\rho \bar{U}\bar{U})$$

If we want to solve the equations for the mean velocity, U, we need to have a model for Reynold's stress, or we must express Reynold's stress in terms of quantities that we know. The most popular method is the application of the Boussinesq hypothesis. In this hypothesis, we relate Reynold's stress to the Mean velocity Gradient.

$$-\rho\bar{U}\bar{U} = \mu_t\big((\nabla V) + (\nabla V)^T\big) - \frac{2}{3}\rho k I - \frac{2}{3}(\nabla \cdot \mathrm{V})I$$

However, to close the equation the calculation of μ_t must be performed. μ_t is known as Eddy viscosity. The expression of the Eddy viscosity is shown below:

$$\mu_t = C_\mu \frac{\rho k^2}{\in}$$

Here, the expressions of k and ∈ are turbulence kinetic energy and turbulence dissipation rate respectively. Thus, we need to solve a transport equation for both of these values to define them and afterward placing in the expression above obtain the value of μ_t. Below we see expressions of turbulence kinetic energy and turbulence dissipation rate. Note that turbulence kinetic energy expression is the same for all of the $k - \epsilon$ methods, however, the ϵ expression changes for each case.

$$\frac{\partial(\rho k)}{\partial t} + \nabla \cdot (\rho V k) = \nabla \cdot \left[\left(\mu + \frac{\mu_t}{\sigma_k}\right) \nabla \mathrm{k}\right] + P_k + P_b - \rho\epsilon + S_k$$

Here P_k is the production due to mean velocity share, P_b is the production due to buoyancy, and S_k is a user-defined source term. Here in the Source part, we see also $\rho\epsilon$ part which is the dissipation rate, and it has a negative sing. It means that the epsilon actually tries to dissipate the turbulent kinetic energy. Below we have the transport equation for turbulence dissipation term:

$$\frac{\partial(\rho\epsilon)}{\partial t} + \nabla \cdot (\rho V \epsilon) = \nabla \cdot \left[\left(\mu + \frac{\mu_t}{\sigma_{k\epsilon}}\right) \nabla \epsilon\right] + C_1 \frac{\epsilon}{k}(f_1 P_k + C_3 P_b) - f_2 C_2 \rho \frac{\epsilon^2}{k} + S_\epsilon$$

$C1, C2$ and C_μ are empirical coefficients which have a particular value and were defined by Launder & Sharma (1974). f_1, f_2 and f_μ are the damping functions which were with the following expressions. So, we must have some way to damp our dissipation rate close to the wall as we did for Damping Functions. There are several types of damping functions, however, below we illustrate the ones for standard $k{-}\in$.

$$f_1 = 1; \quad f_2 = 1 - 0.3ext(-Re_T^2); \quad f_3 = \exp\left(-\frac{3.4}{1 + \left(\frac{Re_T}{50}\right)^2}\right)$$

They damp the dissipation rate close to the wall, which is related to the fact that in the regions closer to the there is a presence of viscous sub-layer in which we have a high impact of viscous effects. In the shown expressions we also see the term ReT. This is called the Turbulent Reynolds number. It is defined as the ratio between turbulent forces and viscous forces:

$$Re_T = \frac{\rho k^2}{\mu \epsilon}$$

3.8.2 k-ω SST model

As was said in the case of the $k - \epsilon$ model, in the RANS equations turbulent/eddy viscosity (μ_t) is being used to close the momentum equations. It accounts for an additional mixing term provided by the turbulence fluctuation. When we switch from the $k - \epsilon$ to the $k - \omega$ model, the kinetic energy term doesn't change, however, the epsilon equation is modified. The reason for the usage of the $k - \omega$ method is coming from the fact that the $k - \epsilon$ method doesn't yield good results when it comes to boundary layers with adverse pressure gradients. Therefore, for the analysis of aerodynamic problems and turbomachinery, it is preferred to use the $k - \omega$ method. We have defined ϵ to be the rate at which the turbulent kinetic energy is converted into thermal energy by viscosity. Below we demonstrate the expression of a specific dissipation rate, ω:

$$\omega = \frac{\epsilon}{C_\mu k} \qquad C_\mu = 0.09$$

As it can be seen, there is a direct relation between specific dissipation rate and dissipation rate, however, their units are different. Another important piece of information that can be taken from the expression is that this expression gives us the freedom of convergence between two indicated terms. For the specific dissipation rate the following transport theorem is given:

$$\frac{\partial(\rho\omega)}{\partial t} + \nabla \cdot (\rho U \omega) = \nabla \cdot \left(\left(\mu + \frac{\mu_t}{\sigma_k} \right) \nabla \omega \right) + \frac{\gamma}{\nu_t} P_k - \beta \rho \omega^2$$

However, the main difference between methods comes from the used empirical coefficients which are different for both variables. the $k - \epsilon$ method uses damping functions closer to wall regions where viscous effects are dominating over turbulence forces, therefore, the size of eddies decreases. However, these damping functions don't work accurately, therefore, the model doesn't perform well in the indicated regions. Unlike, the $k - \epsilon$ model, $k - \omega$ doesn't use any damping function for the determination of dissipation at near-wall regions.

Nevertheless, the $k - \omega$ model also has some weaknesses. The most significant one is the fact that the model depends on freestream turbulence conditions. If the inlet of freestream gives different values of k to our model, we will get different outcomes for μ_t/μ . Also, skin friction coefficient, C_f, obtain different values because of the indicated modifications. In return, it will affect the forces on the body and flow separation inception. This is a problem related to the empirical coefficients used for the case of $k - \omega$.

However, the $k - \epsilon$ model is not as susceptible to the freestream values of k, ω, and ϵ. Therefore, the solution to the problem could be of using k-ϵ at freestream and k-ω in the regions close to the wall. This blending method of application of both methods is called the k-ω BST model.

$$\frac{\partial(\rho\omega)}{\partial t} + \nabla \cdot (\rho U \omega) = \nabla \cdot \left(\left(\mu + \frac{\mu_t}{\sigma_k} \right) \nabla \omega \right) + \frac{\gamma}{\nu_t} P_k - \beta \rho \omega^2 + \frac{2\rho\sigma\omega^2}{\omega} \nabla \mathrm{k} : \nabla \omega$$

This is the expression of dissipation term written in terms of specific dissipation rate. We see the generation of the additional terms in the case of the $k - \omega\ BST$ model. As can be seen from the expression above, this is different from the expression of the k-ω model. That is, the generation of the additional terms comes from the $k - \epsilon$ model. With the application of the blending function, the transport equation is made feasible for both models.

$$(1 - F_1) \frac{2\rho\sigma\omega^2}{\omega} \nabla k : \nabla \omega$$

At the regions closer to the wall F_1 is equal to 1, and thus we obtain the expression of k-ω, however, at freestream, F_1=0, thus leading to the $k - \epsilon$ model. Each cell possesses its own F_1 values. However, the k-ω BST model still overpredicts the wall share stress. To further better the method a viscosity limiter is being added to the model. It limits the viscosity in the regions closer to a wall. Thus, we obtain the method called $k - \omega\ STT$. For this model, the expression of turbulence viscosity is modified through a max limiter:

$$\mu_t = \frac{a_1 \rho k}{\max(a_1 \omega, S F_2)}$$

F_2 is another blending function similar to F_1. When the multiplication of SF_2 gives a large value, then our expression is limited, which indicates of near-wall location.

3.8.3 Results of k-ϵ standard model

As was noted before, further calculations and comparisons of two different models are conducted on fine mesh. In the case of the $k-\epsilon\ Standart$ model, we have defined the values which have been demonstrated above. For this case, average and maximum speeds were defined to be 2.75217m/s and 4.313m/s correspondingly. However, in this chapter, for a better understanding, of the performance of the air channel, the velocity output of each channel will be examined separately and the average speed for each channel will be defined. Below the average velocity value for all outlets of the air channel was demonstrated:

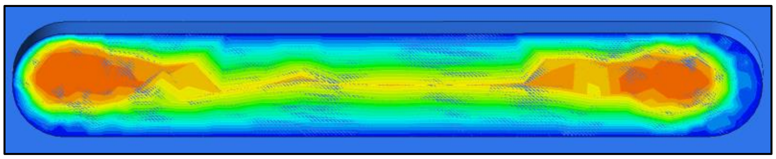

Figure 3.31 Outlet section of the mesh

Outlet section number	Average speed (m/s)	Outlet section number	Average speed (m/s)	Outlet section number	Average speed (m/s)	Outlet section number	Average speed (m/s)
1	2.641	8	2.676	15	2.706	22	2.845
2	2.652	9	2.711	16	2.745	23	2.814
3	2.672	10	2.581	17	2.751	24	2.796
4	2.664	11	2.658	18	2.777	25	2.809
5	2.655	12	2.704	19	2.770	26	2.824
6	2.647	13	2.705	20	2.819	27	2.785
7	2.697	14	2.697	21	2.875	28	2.777

Table 3.24 Average speed value for all outlet sections for k-ϵ turbulence model

Also, the total body is cut through with planes in 18 different points and velocity values for each section are. The first section starts from the frontal part of the bass and goes up to the rare part. Planes are taken from the middle points of outlet sections.

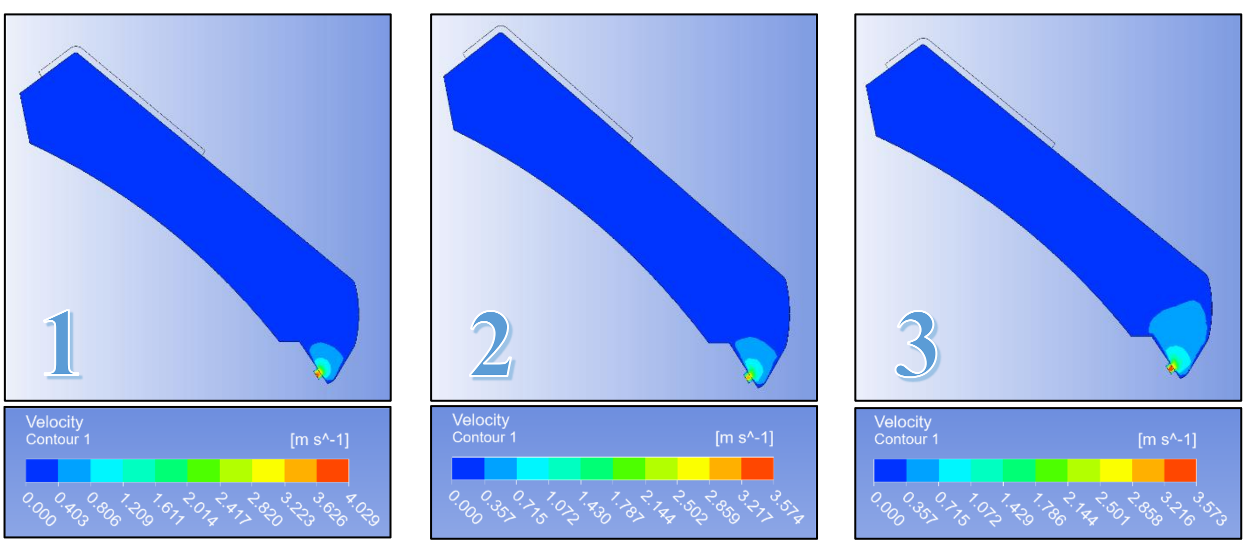

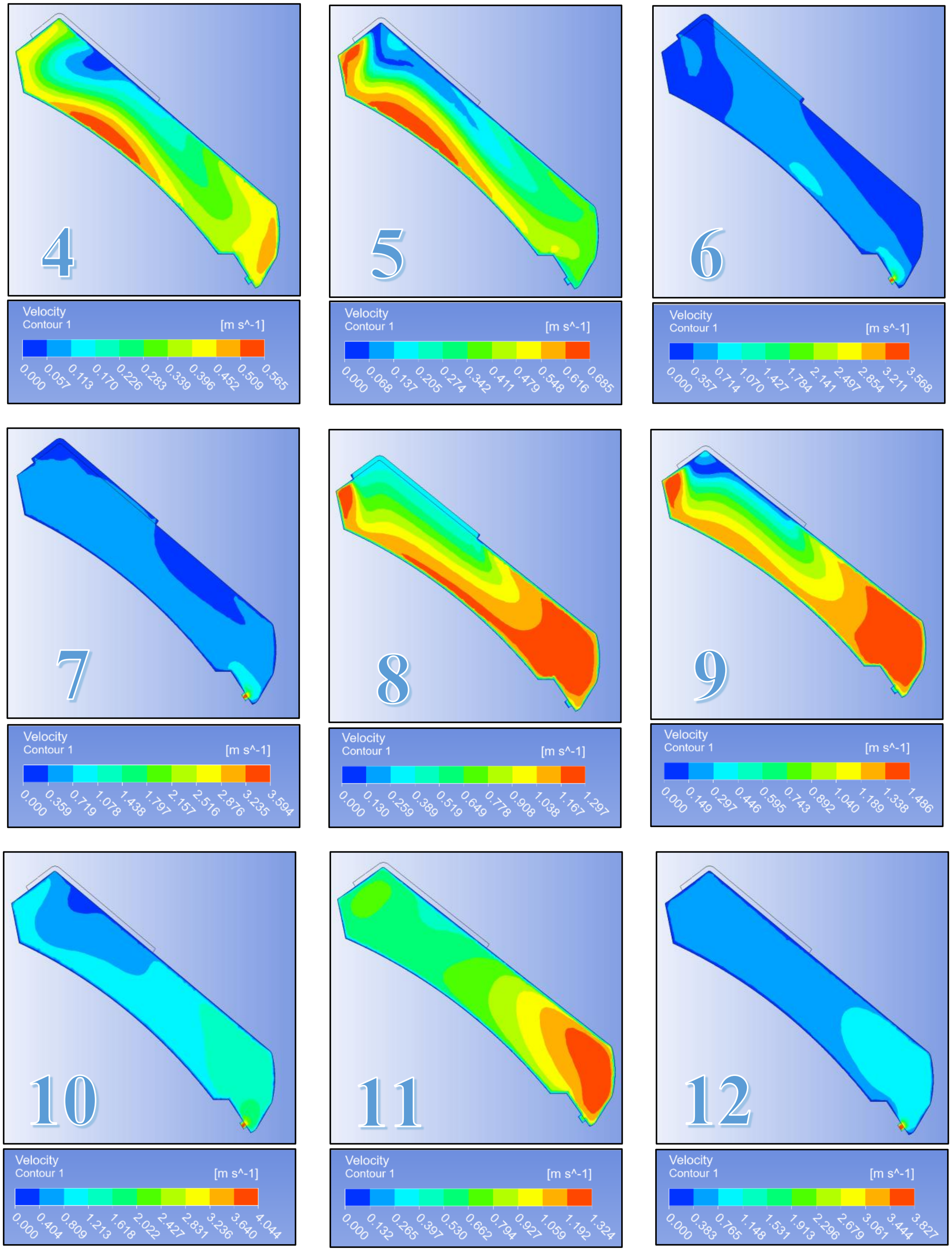
4
Velocity
Contour 1
[m s^-1]
0.000 0.057 0.113 0.170 0.226 0.283 0.339 0.396 0.452 0.509 0.565
5
Velocity
Contour 1
[m s^-1]
0.000 0.068 0.137 0.205 0.274 0.342 0.411 0.479 0.548 0.616 0.685
6
Velocity
Contour 1
[m s^-1]
0.000 0.357 0.714 1.070 1.427 1.784 2.141 2.497 2.854 3.211 3.568
7
Velocity
Contour 1
[m s^-1]
0.000 0.359 0.719 1.078 1.438 1.797 2.157 2.516 2.876 3.235 3.594
8
Velocity
Contour 1
[m s^-1]
0.000 0.130 0.259 0.389 0.519 0.649 0.778 0.908 1.038 1.167 1.297
9
Velocity
Contour 1
[m s^-1]
0.000 0.149 0.297 0.446 0.595 0.743 0.892 1.040 1.189 1.338 1.486
10
Velocity
Contour 1
[m s^-1]
0.000 0.404 0.809 1.213 1.618 2.022 2.427 2.831 3.236 3.640 4.044
11
Velocity
Contour 1
[m s^-1]
0.000 0.132 0.265 0.397 0.530 0.662 0.794 0.927 1.059 1.192 1.324
12
Velocity
Contour 1
[m s^-1]
0.000 0.383 0.765 1.148 1.531 1.913 2.296 2.679 3.061 3.444 3.827

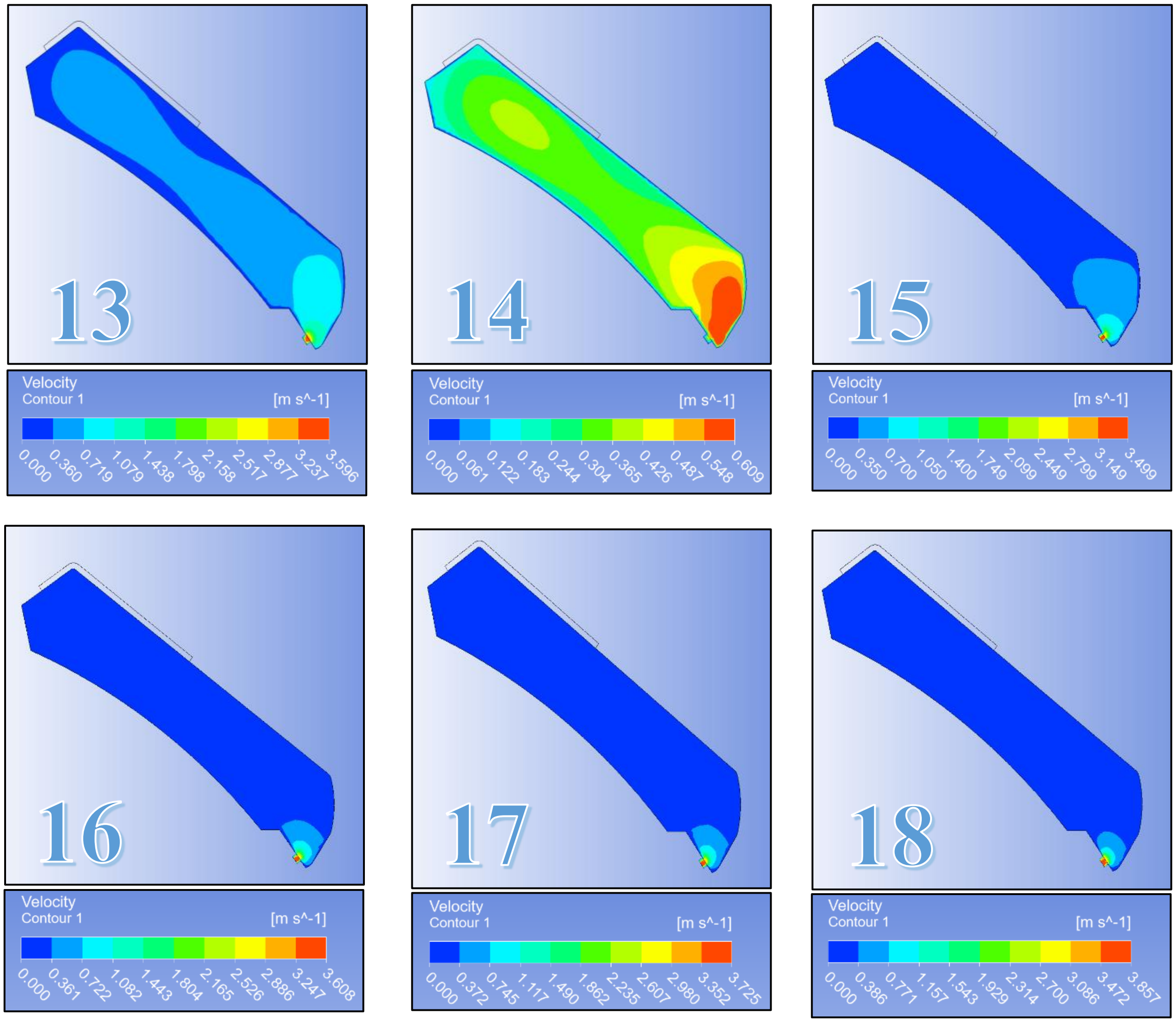

Figure 3.32 Section velocity gradient view of the air channel for k-ϵ model

Below, we see the plane-cut view of our domain.

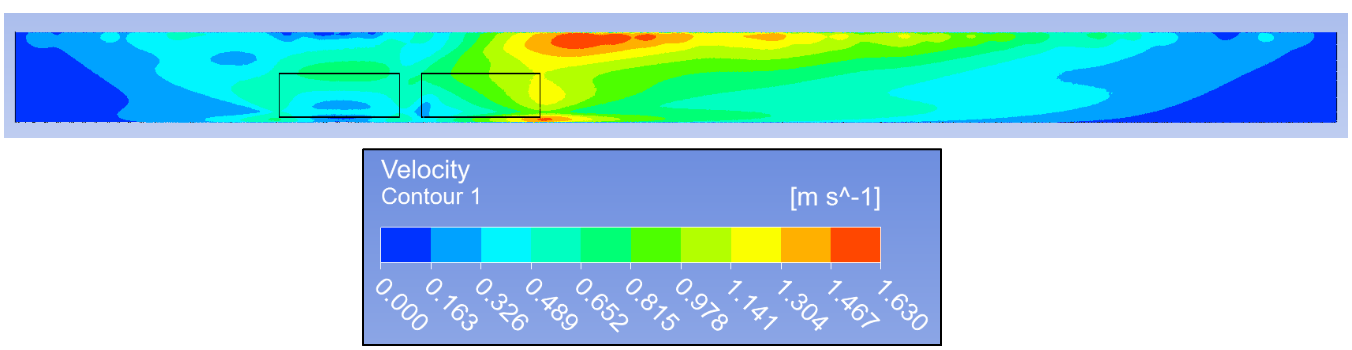

Figure 3.33 Plane cut velocity field view of the air channel for k-ϵ model

Going from the figure shown above, it can be said that the fluid distribution in the channel is not equal which causes the outlet sections closer to the inlet to have higher output speeds compared to ones on rare and frontal parts. Also, through the vector and plot, the direction and distribution of velocity can be examined. AS the vector arrows were not visible in blue font, in this picture the choice of colors for the legend has been changed.

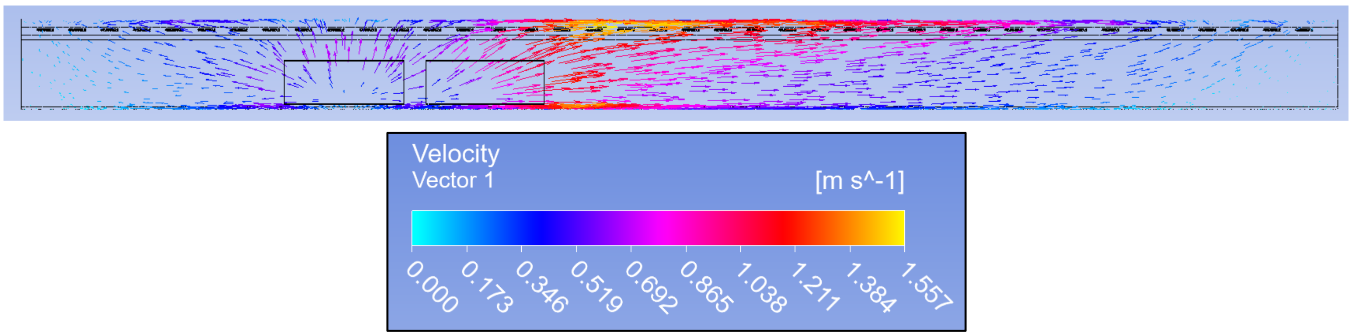

Figure 3.34 Vectorial velocity field view of the air channel for k-ϵ model

3.8.4 Results of k-ω SST model

In the case of the $k - \omega\ SST$ model, the average speed is defined to be 2.69755m/s. Also, the maximum outlet speed is 4.610m/s. Below the average velocity value for all outlets of the air channel was demonstrated:

Outlet section number	Average speed (m/s)	Outlet section number	Average speed (m/s)	Outlet section number	Average speed (m/s)	Outlet section number	Average speed (m/s)
1	2.441	8	2.676	15	2.706	22	2.845
2	2.542	9	2.711	16	2.745	23	2.814
3	2.602	10	2.681	17	2.751	24	2.796
4	2.614	11	2.658	18	2.777	25	2.809
5	2.655	12	2.704	19	2.87	26	2.824
6	2.647	13	2.705	20	2.819	27	2.785
7	2.697	14	2.697	21	2.875	28	2.777

Table 3.25 Average speed value for all outlet sections for k-ω turbulence model

Below, we see the velocity gradient at 18 different sections:

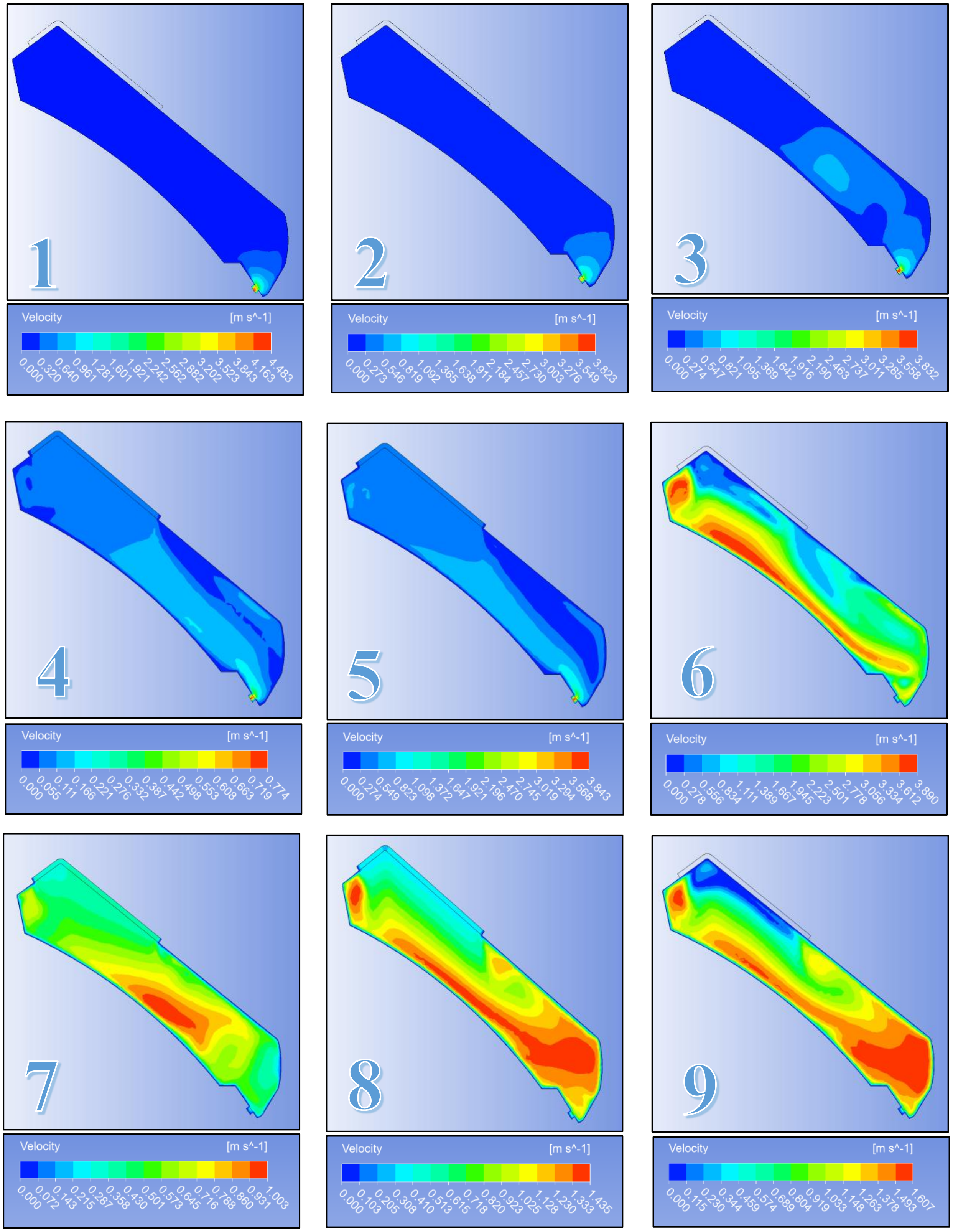

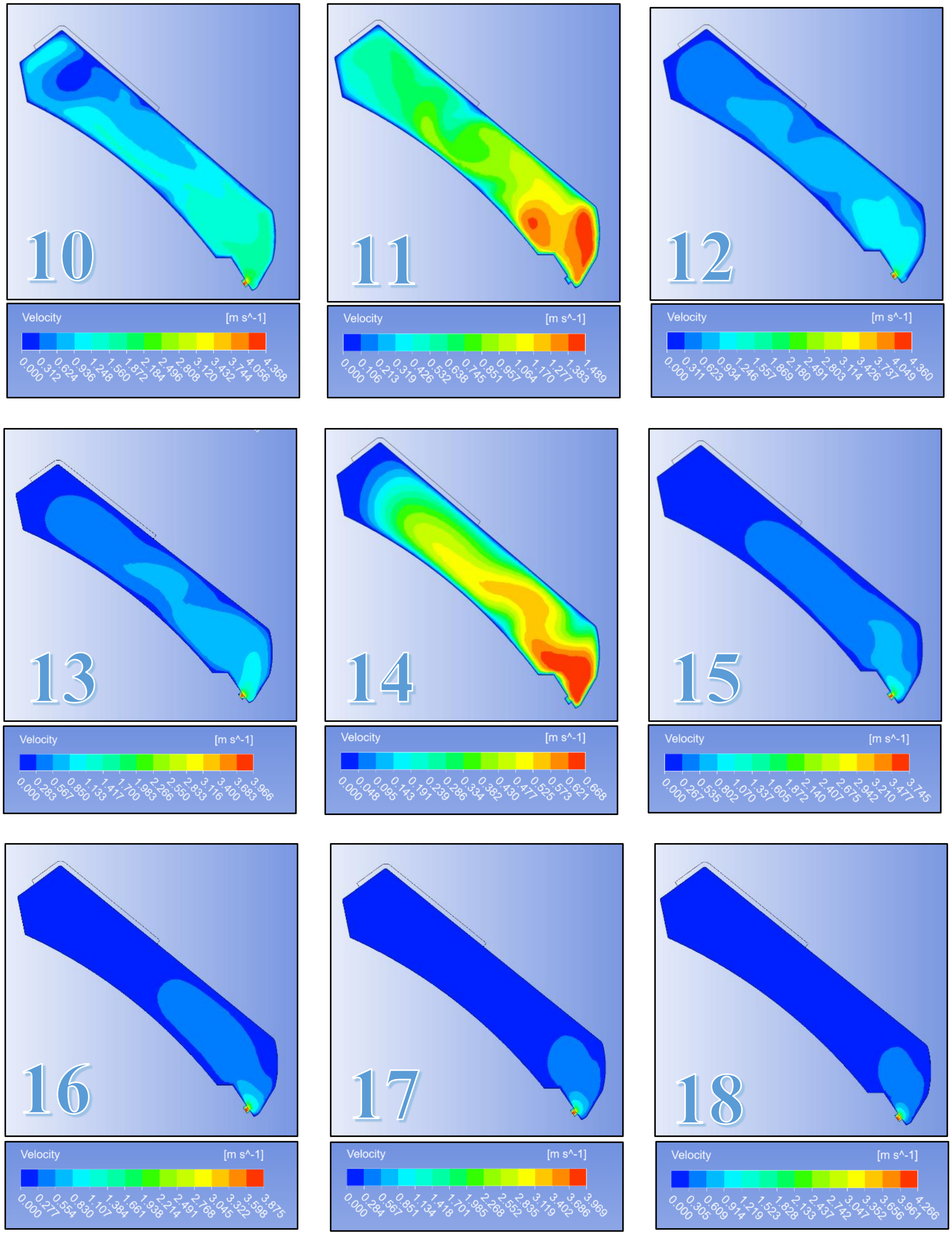

Figure 3.35 Section velocity gradient view of the air channel for k-ω model

Below, we see the plane-cut view of our domain.

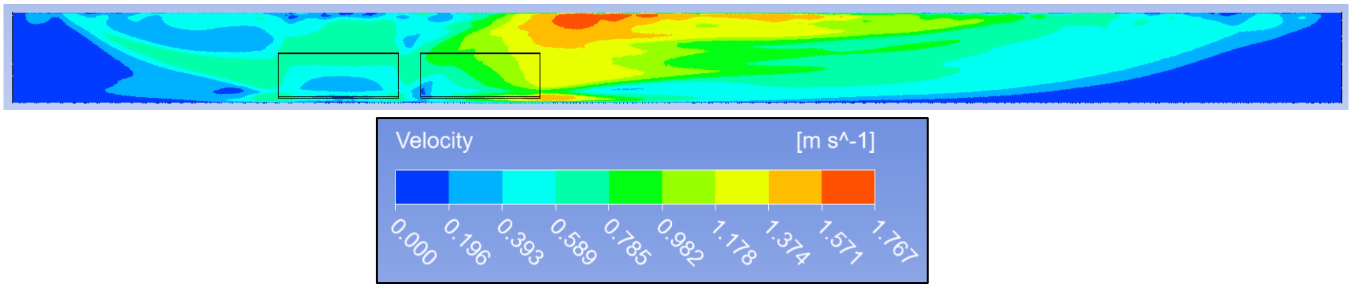

Figure 3.36 Plane cut velocity field view of the air channel for k-ω model

Also, demonstration of vector field for speed components is given below:

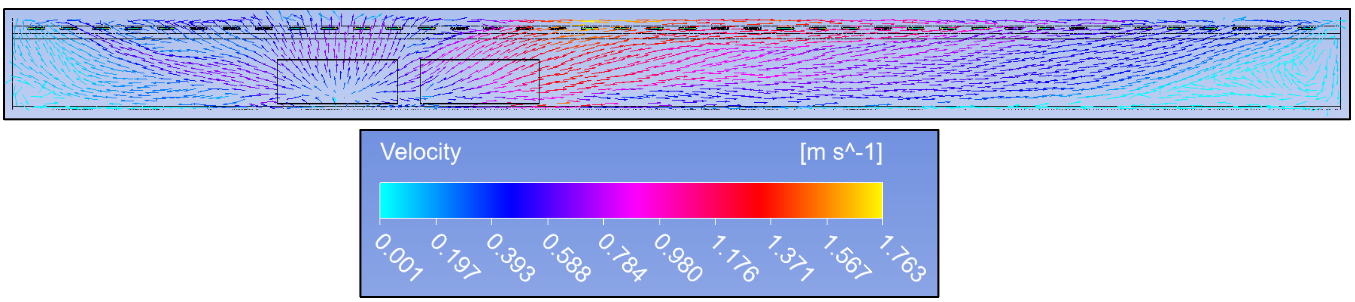

Figure 3.37 Vector plot velocity field view of the air channel with $k - \omega\ SST$ model

3.9 Literature Verification Study

3.9.1 Verification study

For the verification study, a thesis written by Valiev (2021) was used. In this study, the heating, ventilation, and air conditioning (HVAC) air ducts for two different buses with 12 m length, standing and seated passenger capacity of 25 and 62 respectively were examined. For the design of the air duct Catia V5, and for its CFD analysis, SolidWorks programs were used. He examined 2 different buses running with an internal combustion engine and electric motor. Speed, temperature, and pressure distribution in the cabin were studied. With the analysis conducted we tried to decrease cabin temperature from 30 to 16°C.

There are several differences between our studies listed below:

- Bus length and capacity of passengers (54 vs 87)
- The air channel length (12m vs 8m)
- Used software program for CFD analysis (Ansys vs SolidWorks)
- The mass flow rate of the inlet ($220m^3/s$ vs $300m^3/s$)

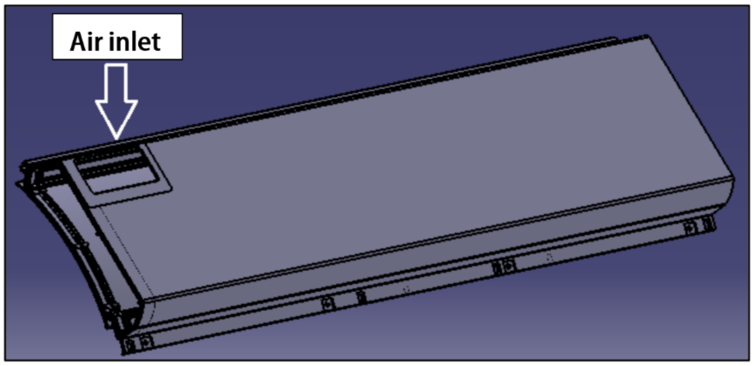

Figure 3.38 Air channel geometry of verification study

3.9.1.1 Comparisons of CFD results for study

Below we have the CFD results comparison. As the bus in our study works with an internal combustion engine, from the literature study also a bus with an internal combustion engine was taken for examination. In both cases in the region closer to the inlet the speed of fluid reaches a maximum value. Also, towards the rare and top sides, the temperature drop is experienced in both cases.

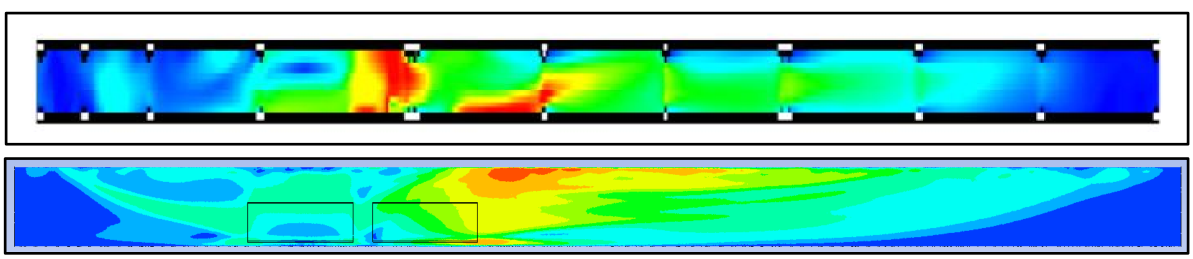

Figure 3.38 Verification of CFD results

Furthermore, in Valiev's CFD study the average speed at the output was 2.5 m/s. In our study, the average speed, taking the output average speed of the k-ϵ Standart model, was defined to be 2.75217m/s. Besides, Valiev's maximum speed component was 3.8m/s which is much higher in comparison with our study's maximum speed, 2.845m/s. For both studies, maximum speed is reached in the outlet region closer to the inlet section.

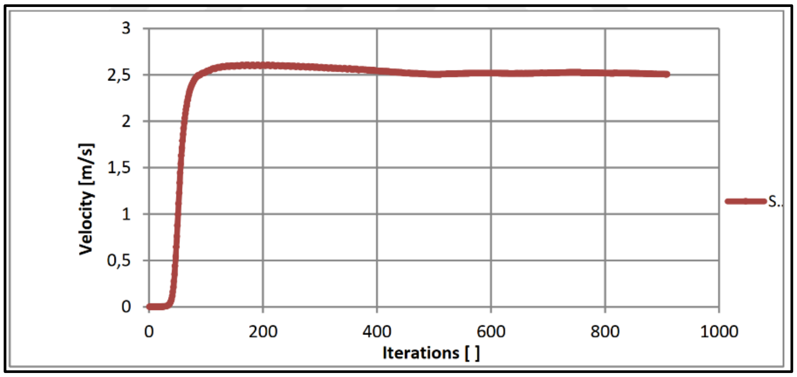

Figure 3.39 Literature study output average speed

3.9.1.2 Experimental results for study

Below the demonstration of experimental results for study is illustrated.

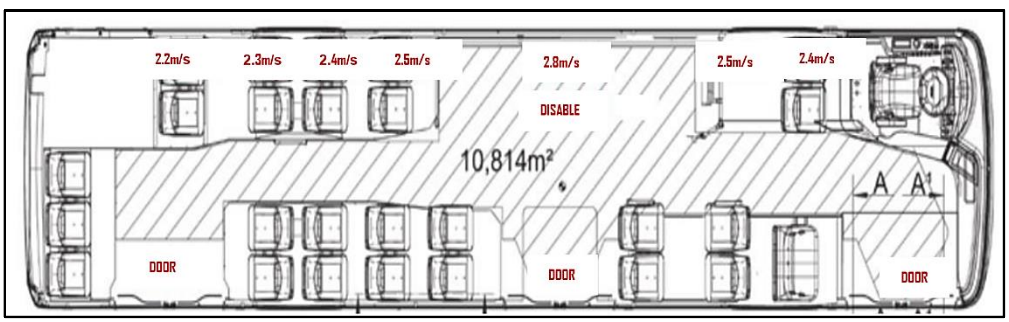

Figure 3.40 Experimental results of Valiev's study

On average, the experimental results of the study accommodate the values given, except for the maximum value which Valiev defined to be 3.8m/s in the CFD study. If the given results are put in comparison with our study, the values at regions are quite comparable with the results of the k-ω SST model, nevertheless, values at the frontal part show an average error of 10%. However, for the case of k-ω Standart, not only the frontal part but also the rare part shows around 14% deviation from the values.

Rare section	Average speed (m/s)
1	2.441
2	2.542
3	2.602
4	2.614
5	2.655
6	2.647
7	2.697
8	2.676
9	2.711
10	2.681
11	2.658
12	2.704
13	2.705
14	2.697

Middle section	Average speed (m/s)
15	2.706
16	2.745
17	2.751
18	2.777
19	2.870
20	2.819
21	2.875
22	2.845
23	2.814
24	2.796
25	2.809
26	2.824

Frontal section	Average speed (m/s)
27	2.785
28	2.777

Table 3.26 Average speed value for all outlet sections for k-ω turbulence model of our study

Rare section	Average speed (m/s)
1	2.641
2	2.652
3	2.672
4	2.664
5	2.655
6	2.647
7	2.697
8	2.676
9	2.711
10	2.581
11	2.658
12	2.704
13	2.705
14	2.697

Middle section	Average speed (m/s)
15	2.706
16	2.745
17	2.751
18	2.777
19	2.770
20	2.819
21	2.875
22	2.845
23	2.814
24	2.796
25	2.809
26	2.824

Frontal section	Average speed (m/s)
27	2.845
28	2.814

Table 3.27 Average speed value for all outlet sections for k-ϵ turbulence model of our study

However, the author did not do experiments for each outlet section of the bus, which is done in this thesis in chapter 4. Also, in this study, the maximum speed achieved in the CFD study and experimental results are quite different, with an error of 26%. The author justified it by the possible assembly gaps which lead to leakages and air.

Chapter 4

Experimental results and comparison outcomes

4.1 Measurement equipment

For the conduction of experiments KINO Hot Wire Thermo-Anemometer was used.

Figure 4.1 Photo of the anemometer

4.2 Experimental measurement process

For validity and comparability of analysis with Computational Fluid Dynamics results the experiment was conducted under particular circumstances.

1. All the doors and windows were closed for clarity
2. To reach the desired temperature (16°C), first, AC system was turned on for 1 hours,
3. The same analysis was conducted on 3 busses with the same branding
4. Analysis was conducted by a calibrated anemometer used by the bus company

Also, several neglections were used:

1. Any air leakage was neglected, thus, there will be no air entry or exit from any surface other than the ventilation holes.
2. Air circulation inside the bus cabin was neglected
3. Radiation coming from sun is neglected
4. It is assumed that the heat loads carried by humans are neglected.

Using the indicated device for each outlet section measurement was conducted. The device can monitor only the first decimal after a point, and besides, it has a particular error that varies between 1-2%.

Figure 4.2 Photo of the anemometer application

B Below we see the results of experimental measurements conducted. As can be seen, the outlet speed of air at the rare part of the bus is smaller compared to the outlet regions closer to the inlet section. The reason for this is the additional engine attached to the frontal part of the channel which sucks air from the channel and delivers it to the driver's cabin. Considering this factor, the designers of the channel found a way out by using of inlet section closer to the frontal part of the air channel.

For certainty of experimental results, the output speed of the air channel was examined in 3 buses. The average value of cases was taken:

Outlet section number	Average speed (m/s)	Outlet section number	Average speed (m/s)	Outlet section number	Average speed (m/s)	Outlet section number	Average speed (m/s)
1	2.3	8	2.7	15	2.8	22	2.9
2	2.4	9	2.7	16	2.8	23	2.9
3	2.5	10	2.7	17	2.8	24	2.9
4	2.5	11	2.7	18	2.8	25	2.9
5	2.5	12	2.7	19	2.9	26	2.8
6	2.6	13	2.7	20	2.9	27	2.7
7	2.6	14	2.7	21	2.9	28	2.7

Table 4.1 Experimental speed value for all outlet sections for bus 1

Outlet section number	Average speed (m/s)	Outlet section number	Average speed (m/s)	Outlet section number	Average speed (m/s)	Outlet section number	Average speed (m/s)
1	2.3	8	2.7	15	2.8	22	2.9
2	2.3	9	2.7	16	2.8	23	2.9
3	2.4	10	2.7	17	2.8	24	2.9
4	2.5	11	2.7	18	2.8	25	2.9
5	2.5	12	2.7	19	2.9	26	2.7
6	2.6	13	2.7	20	2.9	27	2.7
7	2.6	14	2.7	21	2.9	28	2.7

Table 4.2 Experimental speed value for all outlet sections for bus 2

Outlet section number	Average speed (m/s)	Outlet section number	Average speed (m/s)	Outlet section number	Average speed (m/s)	Outlet section number	Average speed (m/s)
1	2.3	8	2.6	15	2.8	22	2.9
2	2.4	9	2.7	16	2.8	23	2.9
3	2.4	10	2.7	17	2.8	24	2.9
4	2.5	11	2.7	18	2.8	25	2.8
5	2.6	12	2.7	19	2.9	26	2.8
6	2.6	13	2.7	20	2.9	27	2.7
7	2.6	14	2.7	21	2.9	28	2.7

Table 4.3 Experimental speed value for all outlet sections for bus 3

Outlet section number	Average speed (m/s)	Outlet section number	Average speed (m/s)	Outlet section number	Average speed (m/s)	Outlet section number	Average speed (m/s)
1	2.3	8	2.66	15	2.8	22	2.9
2	2.36	9	2.7	16	2.8	23	2.9
3	2.43	10	2.7	17	2.8	24	2.9
4	2.5	11	2.7	18	2.8	25	2.86
5	2.53	12	2.7	19	2.9	26	2.76
6	2.6	13	2.7	20	2.9	27	2.7
7	2.6	14	2.7	21	2.9	28	2.7

Table 4.4 Experimental average speed value for all outlet sections of three examined busses

As a result of the experiments, the average speed at bus outlet is defined to be 2.70714 m/s.

4.3 The comparison of accuracy of the methods

As it can be seen from the tables above, the experimental results have given us the output speed of fluid to be equal to 2.70714m/s which is slightly different from the outputs of $k-\epsilon$ and $k-\omega\, SST$ methods, which yielded 2.75217m/s and 2.69755m/s correspondingly. Thus, the CFD study errors for $k-\epsilon$ and $k-\omega\, SST$ methods can be defined as 1.64% and 0.35% correspondingly. However, besides the total output errors, the error for each output also plays an important role. Below the demonstration of error for each outlet section have been given.

Outlet section number	Error value (%)	Outlet section number	Error value (%)	Outlet section number	Error value (%)	Outlet section number	Error value (%)
1	8.6939	8	0.6015	15	5.5409	22	1.3631
2	12.3728	9	0.2954	16	2.4515	23	0.5896
3	9.9588	10	0.4090	17	1.7811	24	5.2249
4	3.3255	11	4.6106	18	1.5228	25	1.7832
5	4.9407	12	1.3513	19	6.5393	26	2.3188
6	0.6581	13	1.6566	20	3.0561	27	2.1566
7	0.9146	14	1.0101	21	0.0344	28	0.2227

Table 4.5 Error values of each outlet section for $k-\epsilon\ Standart$

Outlet section number	Error value (%)	Outlet section number	Error value (%)	Outlet section number	Error value (%)	Outlet section number	Error value (%)
1	5.7763	8	0.6015	15	3.4737	22	1.9332
2	7.7118	9	0.4057	16	2.0036	23	3.0561
3	7.0781	10	0.7086	17	1.7811	24	3.7196
4	4.3611	11	1.5801	18	0.8282	25	1.7832
5	4.9407	12	0.14792	19	1.0453	26	2.3188
6	1.7755	13	0.1848	20	2.8733	27	3.0520
7	3.5965	14	0.1112	21	0.8695	28	2.7727

Table 4.6 Error values of each outlet section for $k-\omega\ SST$

According to the values given in the tables, we can solidly define that the $k-\omega\, SST$ method has shown better performance in the prediction of outlet values. Especially, at the outlet sections closer to the rare part of the bus $k-\epsilon\ Standard$ method has given results with a high deviation from the original value. Of course, there are other reasons for high deviation such as possible leakages of the assembly and geometrical simplifications done on the geometry. Furthermore, the measuring device also has a particular measurement efficiency, which varies between 1-2%.

The images shown in CFD results show us that the distribution of air inside the channel is not even, and as the inlet part is located far away from the rare part, at the rare part the speed of air is comparatively. In addition, outlet sections that are in alignment with the inlet section possess higher air output velocity. To overcome this problem, as can be seen from the image below, some outlet sections are closed, which results in better distribution of air inside the channel.

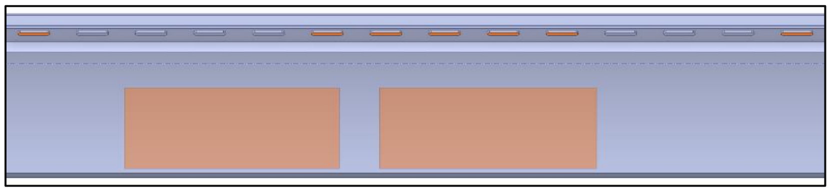

Figure 4.3 Inlet section of the air channel

The reason for this positioning of inlet sections is because on the frontal part of the channel there is an additional exit that feeds the driver seat. However, as the air channel cooling is sufficient for the thermal comfort of both passengers and drivers, mostly the additional air-sucking is turned off.

4.4 Suggestions on better performance of the air channel

There can be several suggestions for improvement of the efficiency and effectiveness of the air distribution and one of them is the change in the position of inlet sections and distributing them on the channel at different positions. However, to have this kind of design work optimally, the 2 feeding channels, for each of the inlet sections, must have different air flow rates. When driver local cooling is turned off, both inlet sections distribute the same amount of air into the channel, however, when the function is turned on, the inlet section closer to the frontal part will have an additional load to compensate for the loss. However, this application will increase the cost of the cooling system in return causing only a slight change in thermal comfort. Nevertheless, below we see the demonstration of the speed gradient inside the system and at each outlet section with this application. To reach the result faster, $k - \epsilon\ Standard$ has been applied.

Figure 4.4 Feeding channels of air-channel

Figure 4.6 Suggested design of air channel

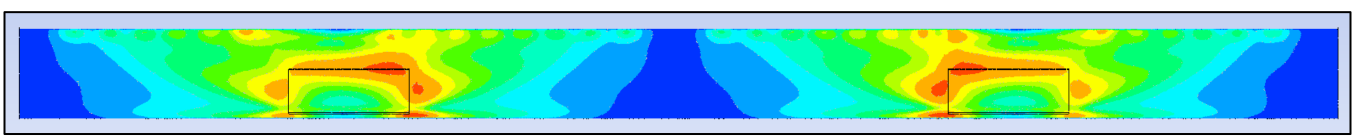

Figure 4.7 Air velocity distribution in channel with suggested design

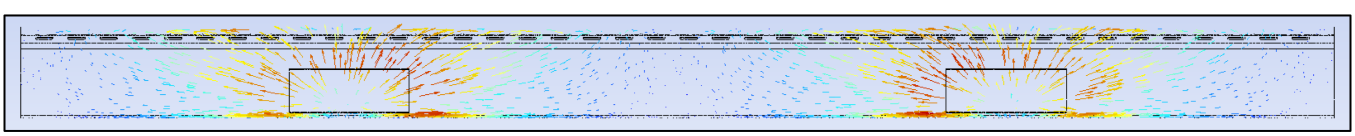

Figure 4.8 Vector view of air velocity distribution in channel with suggested design

Outlet section number	Average speed (m/s)	Outlet section number	Average speed (m/s)	Outlet section number	Average speed (m/s)	Outlet section number	Average speed (m/s)
1	2.666	8	2.670	15	2.704	22	2.686
2	2.703	9	2.658	16	2.694	23	2.669
3	2.693	10	2.682	17	2.693	24	2.664
4	2.688	11	2.691	18	2.683	25	2.686
5	2.692	12	2.708	19	2.671	26	2.695
6	2.688	13	2.692	20	2.675	27	2.695
7	2.726	14	2.694	21	2.681	28	2.701

Table 4.7 Output speed values for suggested design

As it can be seen from the output values for the suggested design the values at the output are quite close to each other. The maximum and minimum output values for this case are 2.708m/s and 2.658m/s. According to these values, the difference is 1.846%.

However, for the case of the original design, with the same $k - \epsilon\ Standard$ method, the maximum and minimum values were defined to be 2.581 and 2.875. Thus, the difference in percentage for the original design is 10.22%.

References

Boltz. N., Schaller. R., and Scheid. H., 2011. AC Systems for Buses and Coaches.

Carrier, 2004. Air Conditioning System Design, Part 2, Alarko Carrier Publications, Istanbul.

Asghar. H. B. (2016). New design of bus Air channels through finite element method. Isparta: SDÜ FBE.

Atmaca, İ. (2015). Cooling of intercity buses and air quality.

Körbahtı, B. 1999. CFD of Climatization Processes in Inter-City Buses, MSc Thesis, İstanbul University, Institute of Natural and AS.

Belkıs Erzincanlı Süsler, H. A. (2016). Air Duct Design Iterations to Improve Defog Performance. 8. Otomotiv Teknolojileri Kongresi (s. 1). Bursa: Otekon'16.

Ekeroth, F., And Martinsson, A., 2011. Fluid dynamics section of the department of applied mechanics' numerical simulations of big trucks under hood flow employing pans, Chalmers University of Technology.

Bayraktar, I., 2012. Methods of Computational Simulation for Vehicle Thermal Control, Applied Thermal Engineering.

Menter F.R – Models of Two-Equation Eddy Viscosity for Engineering Applications. AAIA Journal, Vol 32, No.88, August 1994.

Apsley D.D – Leschziner, M.A – Advanced turbulence modeling of separated flow in the diffuser

Flow, Turbulence and Combustion 2000.

Xıao, G., Yang, Z., Wang, D., And Zhang, W., 2008. The Underbody of a Vehicle Radiation and Conjugate Heat Transfer Investigation, SAE Technical Paper 2008-01-1819.

Somanı, A., 2008. Energy-efficient Data Centers Using Advanced Thermal Management Strategies, MSc. Thesis, School of G.W. Woodruff School of Mechanical Engineering.

Mezarcıöz, S. (2015). Improving the Air Conditioning System of a Passenger Bus with the Application of a Separate Air Duct.

Pala, U. (2020). Examination of the bus passengers' thermal comfort during a cooling test inside a climate control room. Journal of Polytechnic.

Fırat Ekinci, A. E. (2019). Thermodynamic analysis of an intercity bus AC System working with HCFC, HFC, CFC, and HC refrigerants. International Journal of Automotive Engineering and Technologies.

Sevilgen, G. (2010). Three-Dimensional Numerical Analysis of Speed and Temperature Distribution in an Automobile Cabin. Bursa: Uludağ University FBE.

Srinivasa Yenneti, G. N. (2014). AC system optimization for a roof-top bus powered by the primary engine. International Refrigeration and Air Conditioning Conference (s.1).

Standard, A. (2010). Temperature Requirements for Human Occupancy. Atlanta: American Society of Heating, Refrigerating and Air-Conditioning Engineers, Inc

Dr Aidan Wilmshurst. Computational observations of the tip loss mechanism experienced by horizontal axis rotors Wind Energy, 2018.

Fundamentals of Fluid dynamics for engineering (Cengel and Cimbala's Fluid Mechanics)

Christopher Rumsey – NASA Langley Research Center – Turbulence Modelling Resources

NASA Turbulence Modelling Resource: turbmodels.larc.nasa.gov

ERCOFTAC Knowledge Base Wiki: kbwiki.ercoftac.org/w/index.php?title=Main_Page

Makina, T. (2020). Hava Kanalları: www.teknikmakina.com/hava-kanallari

CFD Online Wiki: www.cfd-online.com/Wiki/Validation_and_test_cases